

# Nonadiabatic effects in the photoelectron spectrum of the pyrazolide- $d_3$ anion: Three-state interactions in the pyrazolyl- $d_3$ radical

Takatoshi Ichino, Adam J. Gianola, and W. Carl Lineberger<sup>a)</sup>

*JILA, University of Colorado and National Institute of Standards and Technology, Boulder, Colorado 80309-0440 and Department of Chemistry and Biochemistry, University of Colorado, Boulder, Colorado 80309-0440*

John F. Stanton<sup>b)</sup>

*Institute for Theoretical Chemistry, Department of Chemistry and Biochemistry, University of Texas, Austin, Texas 78712*

(Received 1 June 2006; accepted 25 July 2006; published online 28 August 2006)

The 351.1 nm photoelectron spectrum of the 1-pyrazolide- $d_3$  anion has been measured. The photoelectron angular distributions indicate the presence of nearly degenerate electronic states of the 1-pyrazolyl- $d_3$  radical. Equation-of-motion ionization potential coupled-cluster singles and doubles (EOMIP-CCSD) calculations have been performed to study the low-lying electronic states. The calculations strongly suggest that three electronic states, energetically close to each other, are accessed in the photodetachment process. Strong interactions of the pseudo-Jahn-Teller type in each pair of the three states are evident in the calculations for the radical at the anion geometry. Model diabatic potentials of the three states have been constructed around the anion geometry in terms of the anion reduced normal coordinates up to the second order. An analytic method to parametrize the quadratic vibronic coupling (QVC) model potentials has been introduced. Parameters of the QVC model potentials have been determined from the EOMIP-CCSD and CCSD(T) calculations. Simulations of the 1-pyrazolide- $d_3$  spectrum have been performed with the model Hamiltonian, treating all vibronic interactions amongst the three states simultaneously. The simulation reproduces the fine structure of the observed spectrum very well, revealing complicated nonadiabatic effects in the low-lying states of the radical. The ground state of the 1-pyrazolyl- $d_3$  radical is  ${}^2A_2$  and the electron affinity is  $2.935 \pm 0.006$  eV. The first excited state is  ${}^2B_1$  with a term energy of  $32 \pm 1$  meV. While the high-symmetry ( $C_{2v}$ ) stationary points of the  $\tilde{X} {}^2A_2$  and  $\tilde{A} {}^2B_1$  states are minima, that of the  $\tilde{B} {}^2B_2$  state is a saddle point as a result of the pseudo-Jahn-Teller interactions with the other two states. The topology of the adiabatic potential energy surfaces is discussed. © 2006 American Institute of Physics. [DOI: 10.1063/1.2338043]

## I. INTRODUCTION

We have recently conducted a series of investigations on five-membered carbon-nitrogen heterocyclic compounds in order to better understand the effects of nitrogen versus carbon atoms on the electronic and thermochemical properties of these species.<sup>1–3</sup> Photoelectron spectroscopy of the deprotonated anions has provided information on the vibronic structure of low-lying electronic states of the corresponding neutral radicals. Particularly interesting vibronic features have been found for the 1-pyrazolyl- $h_3$  radical.<sup>3</sup> The photoelectron angular distributions indicate that the electronic ground and first excited states of 1-pyrazolyl- $h_3$  are separated adiabatically by only  $32 \pm 1$  meV. While such a near degeneracy is expected on the basis of electronic structure calculations, Franck-Condon (FC) simulations based on the results of density functional theory (DFT) calculations [B3LYP/6–311++G( $d,p$ )] fail to satisfactorily reproduce the observed spectrum.<sup>3</sup> Such a failure is not surprising if the electronic states are subject to large nonadiabatic interac-

tions. In the present study, we explore nonadiabatic effects in the low-lying states of the 1-pyrazolyl radical.

The model diabatic Hamiltonian technique, as advocated and developed by Köppel *et al.*,<sup>4</sup> has been widely used to study nonadiabatic effects in spectroscopy. A number of photoelectron as well as electronic absorption spectra have been analyzed with this approach, which have found varying degrees of success.<sup>5–29</sup> Application of the model Hamiltonian technique to the 1-pyrazolyl radical is especially challenging because of the large number of active normal modes that need to be included in the model potential energy functions. This radical has three close-lying electronic states that interact nonadiabatically with each other.<sup>3,30,31</sup> There have only been a few studies reported in the literature that analyze spectroscopic manifestation of vibronic coupling between three nearly degenerate (or degenerate) states.<sup>19,25</sup> Meanwhile, nonadiabatic effects on photochemistry due to a three-state conical intersection have been a topic of recent theoretical studies.<sup>32–34</sup>

In the present study of the nonadiabatic effects in 1-pyrazolyl, we have measured the photoelectron spectrum of the 1-pyrazolide- $d_3$  anion. The 1-pyrazolyl- $d_3$  radical

<sup>a)</sup>Electronic mail: wcl@jila.colorado.edu

<sup>b)</sup>Electronic mail: stanton@jfs1.cm.utexas.edu

turns out to be a better system for this study than the normal isotopomer because the vibronic coupling scheme is simpler in the model potentials; this simplification allows the full three-state interaction problem to be computationally tractable. In this work, we report an analysis of nonadiabatic effects in the photoelectron spectrum of the 1-pyrazolide- $d_3$  anion, using the model Hamiltonian technique.

It is important to choose an appropriate electronic structure method to evaluate nonadiabatic couplings in order to provide an accurate picture of nonadiabatic effects in spectra. The equation-of-motion coupled-cluster methods<sup>35,36</sup> are well suited for this purpose, as the wave functions can handle multireference effects while dynamic electron correlation is also taken into account.<sup>37</sup> The equation-of-motion ionization potential coupled-cluster singles and doubles (EOMIP-CCSD) method<sup>36</sup> is employed in our study to parametrize the model potentials. This method has been applied successfully in the past for spectral simulations.<sup>21,22,26–28</sup>

It is known that a qualitative understanding of the nonadiabatic effects manifest in spectra can be achieved with a so-called linear vibronic coupling (LVC) approximation of the model potentials.<sup>4</sup> Recently, a number of studies have been reported in the literature where higher-order terms are included to improve the quality of the simulations.<sup>12,16,19,24–27</sup> We employ a quadratic vibronic coupling (QVC) model in the present study and provide a full description of the parametrization of the QVC model. This parametrization, which we call the “adiabatic parametrization” in this paper, is similar to that used in conventional FC overlap calculations<sup>38,39</sup> with respect to the Duschinsky mode mixing.<sup>40</sup> In order to compare the performance of the adiabatic parametrization with that of the parametrization method usually used (i.e., the “vertical parametrization”), the photoelectron spectrum of the 1-imidazolide anion<sup>2</sup> is studied. The 1-imidazolyl radical is a structural isomer of 1-pyrazolyl, but exhibits considerably less profound nonadiabatic effects in its spectrum.<sup>2</sup> The adiabatic parametrization gives a better simulation of the 1-imidazolyl spectrum than the vertical parametrization. Subsequently, we find that our simulation reproduces the spectrum of the 1-pyrazolide- $d_3$  anion very well, revealing complicated nonadiabatic effects in the low-lying states of the 1-pyrazolyl- $d_3$  radical.

This article is organized as follows. In Sec. II, a brief description of negative ion photoelectron spectroscopy is given. Details of the computational methodology are described next, namely, electronic structure calculations and spectral simulations with the model Hamiltonian. In Sec. III the photoelectron spectrum of the 1-imidazolide anion is simulated with the model Hamiltonian technique to test our parametrization method for a related, albeit simpler, problem. Then, nonadiabatic effects in the photoelectron spectrum of the 1-pyrazolide- $d_3$  anion are analyzed systematically, with vibronic interactions within each pair of the three low-lying states of the 1-pyrazolyl- $d_3$  radical studied individually. With the full, three-state nonadiabatic simulation, unambiguous assignments of the electronic states of the 1-pyrazolyl- $d_3$  radical are greatly facilitated. Reasonable assignments are also given to the observed vibronic peaks. An analysis of the photoelectron spectrum of the 1-pyrazolide- $h_3$

anion is provided in the supplementary materials.<sup>41</sup> In Sec. IV, the applicability of the model Hamiltonian method to this complicated nonadiabatic system is discussed. The topology of the potential energy surfaces and conical intersections are discussed as well. Section V presents our conclusion.

## II. METHODS

### A. Experimental procedure

Details of the photoelectron spectrometer have been described in the literature,<sup>42–44</sup> and experimental procedures for the measurements of photoelectron spectra of the 1-pyrazolide- $d_3$  anions are virtually identical to those given in our previous paper.<sup>3</sup> Briefly, atomic oxygen anion ( $O^-$ ) is generated by microwave discharge in a helium buffer gas at  $\sim 0.4$  Torr with a trace amount of oxygen in a flowing afterglow ion source.  $O^-$  reacts with methane introduced downstream to form the hydroxide anion ( $HO^-$ ). Deuterated pyrazole is introduced into the flow tube further downstream and reacts with  $HO^-$  to form the 1-pyrazolide- $d_3$  anion. The ions are thermalized through collisions with the He buffer gas in the flow tube. The flow tube is cooled with liquid nitrogen so that thermal equilibration leads to an ion temperature of  $< 200$  K. The ions are extracted into the low pressure region, accelerated to 740 eV, and focused into a Wien velocity filter. The mass-selected ion beam is refocused and decelerated to 35 eV into the interaction region where it crosses an argon ion laser beam operating at 351.1 nm (3.531 eV) with  $\sim 100$  W of circulating power in an external buildup cavity. A typical beam current for the pyrazolide ion is  $\sim 100$  pA. Of all the photoelectrons, those emitted in a small solid angle around the axis perpendicular to both the ion and laser beams are collected for the kinetic energy analysis. After passing through the hemispherical energy analyzer, the photoelectron signals are amplified via microchannel plates and detected on a position sensitive detector. The kinetic energy resolution is 8–10 meV. The photoelectron spectra are constructed as a function of electron binding energy (eBE), which is the laser energy minus the photoelectron kinetic energy (eKE). The absolute eKE is calibrated by a measurement of the photoelectron spectrum of the iodide anion ( $I^-$ ) with the known electron affinity (EA) of the iodine atom.<sup>45,46</sup> A linear energy compression factor<sup>42</sup> is determined from the measurements of the photoelectron spectra of  $O^-$  and  $I^-$ . A rotatable half-wave plate is placed in the laser beam path so that the angle ( $\theta$ ) between the electric field vector of the laser beam and the photoelectron collection axis can be controlled. The angular dependence of photoelectrons<sup>47</sup> is given by

$$I(\theta) = \frac{\sigma_0}{4\pi} (1 + \beta P_2(\cos \theta)), \quad (1)$$

where  $\sigma_0$  is the total photodetachment cross section,  $\beta$  is the anisotropy parameter, and  $P_2(\cos \theta)$  is the second Legendre polynomial. The photoelectron spectra measured at the magic angle ( $\theta = 54.7^\circ$ ) is free from the angular dependence. The  $\beta$  values are determined from the measurements at  $\theta = 0^\circ$ ,  $90^\circ$ , and the magic angle.

Deuterated pyrazole was prepared according to the literature procedure.<sup>48</sup> In a heavy-wall, borosilicate glass tube

(Ace), 10.0 g of pyrazole (0.15 mol; Aldrich, 98%) was placed with 1.3 ml of 40 wt % NaOD in D<sub>2</sub>O (19 mM NaOD and 59 mM D<sub>2</sub>O; Aldrich, 99.5 at. % D) and 17 ml of D<sub>2</sub>O (0.94 mol; Aldrich 99.9 at. % D). The glass tube was sealed under N<sub>2</sub> atmosphere and heated in an oil bath at 170 °C with stirring. The heating was continued for 10 h. After cooling, the isotopomers of pyrazole were extracted with 50 ml of methylene chloride and 1.5 ml of 37 wt % DCI in D<sub>2</sub>O to neutralize the solution. The methylene chloride extraction was repeated three times. The combined methylene chloride solution was dried over magnesium sulfate. With magnesium sulfate filtered out, methylene chloride was evaporated to obtain partially deuterated pyrazole. The extent of deuteration was checked with gas chromatographic mass spectrometry (GCMS) and <sup>1</sup>H-NMR. The whole procedure was repeated for the partially deuterated sample. After three cycles, the extent of deuterium exchange is 76% in GCMS measurements. The NMR spectrum shows that most of the remaining <sup>1</sup>H (~90%) is located at the N atom. The mass spectrometric measurements for HO<sup>-</sup> reaction with the deuterated pyrazole sample show that 92%–93% of the product ions have *m/z* of 70. It should be remembered that while the majority of HO<sup>-</sup> deprotonates pyrazole at the N atom, a small fraction of HO<sup>-</sup> deprotonates pyrazole at a C atom to produce the 5-pyrazolide anion.<sup>3</sup> Therefore, the extent of replacement of C–H with C–D in pyrazole is >95%, which represents the isotopic purity of the 1-pyrazolide-*d*<sub>3</sub> anion in our photoelectron spectroscopic measurements. We have not noticed contamination of photoelectrons from the 5-pyrazolide anion in the corresponding eKE region of the photoelectron spectra of the 1-pyrazolide-*d*<sub>3</sub> anion.<sup>3</sup>

## B. Electronic structure calculations

The *ab initio* calculations were performed with the ACES II program package.<sup>49</sup> For the 1-pyrazolide and 1-imidazolide anions, the CCSD method<sup>50</sup> was employed to optimize the geometry of the ground states using analytic energy gradients.<sup>51</sup> The quadratic force constants were calculated with analytic second derivatives.<sup>52</sup> For the open-shell systems, i.e., the 1-pyrazolyl and 1-imidazolyl radicals, the EOMIP-CCSD was employed to optimize the geometry of the states of different electronic symmetries, using analytic energy gradients.<sup>36</sup> Finite differences of analytic first derivatives were calculated to obtain the quadratic force constants. In these calculations, the Huzinaga-Dunning double-zeta plus polarization (DZP) basis set<sup>53,54</sup> was used. When potential energies were calculated at single points with a perturbative estimate of triples taken into account [CCSD(T)],<sup>55</sup> the cc-pVTZ basis set of Dunning<sup>56</sup> was used.

Table I shows calculated harmonic vibrational frequencies of the 1-pyrazolide-*d*<sub>3</sub> anion and 1-pyrazolyl-*d*<sub>3</sub> radical. Relative energies of the electronic states of the 1-pyrazolyl radical at the corresponding equilibrium geometry (i.e., adiabatic energies) and at the anion equilibrium geometries (i.e., vertical energies) are given in Table II.<sup>57</sup> The adiabatic energies have been corrected for the zero-point vibrational energies calculated from the harmonic frequencies. Corresponding information for the 1-imidazolyl radical is also provided

TABLE I. Harmonic vibrational frequencies (cm<sup>-1</sup>) of the  $\tilde{X}^1A_1$  state of the 1-pyrazolide-*d*<sub>3</sub> anion and the  $\tilde{X}^2A_2$ ,  $\tilde{A}^2B_1$ , and  $\tilde{B}^2B_2$  states of the 1-pyrazolyl-*d*<sub>3</sub> radical calculated with the CCSD (pyrazolide) and EOMIP-CCSD (pyrazolyl) methods and the DZP basis set.

Mode	Symmetry	1-pyrazolide- <i>d</i> <sub>3</sub>		1-pyrazolyl- <i>d</i> <sub>3</sub>	
		$\tilde{X}^1A_1$	$\tilde{X}^2A_2$	$\tilde{A}^2B_1$	$\tilde{B}^2B_2$
1	<i>a</i> <sub>1</sub>	2423	2487	2458	2494
2		2360	2433	2424	2442
3		1454	1494	1546	1622
4		1222	1413	1184	1377
5		1127	1055	949	1185
6		898	884	883	879
7		790	799	755	809
8	<i>a</i> <sub>2</sub>	698	717	656	600
9		559	492	312	486 <i>i</i>
10	<i>b</i> <sub>1</sub>	675	680	745	618
11		522	562	547	562
12		502	386	389	571 <i>i</i>
13	<i>b</i> <sub>2</sub>	2374	2444	2439	2474
14		1407	1260	1456	1405
15		1347	1135	1188	1273
16		988	873	936	946
17		897	736	737	760
18		714	629	634	540

in Table II. A compilation of other relevant results of electronic structure calculations is available from EPAPS.<sup>41</sup> These include the optimized geometries of the 1-pyrazolide anion, 1-pyrazolyl radical, 1-imidazolide anion, and 1-imidazolyl radical, and the harmonic vibrational frequencies of the 1-pyrazolide-*h*<sub>3</sub> anion, 1-pyrazolyl-*h*<sub>3</sub> radical, 1-imidazolide anion, and 1-imidazolyl radical.

## C. Model Hamiltonian

Nonadiabatic effects in the photoelectron spectra are investigated using the model diabatic Hamiltonian approach advocated and developed by Köppel *et al.*<sup>4</sup> Details of the

TABLE II. Vertical and adiabatic energies (eV) of the 1-pyrazolyl radical and the 1-imidazolyl radical calculated at the EOMIP-CCSD level of theory with the DZP basis set and the CCSD(T) level of theory with the cc-pVTZ basis set. The adiabatic energies have been corrected for the zero-point vibrational energies evaluated from the harmonic frequencies.

	EOMIP-CCSD		CCSD(T)	
	Vertical	Adiabatic	Vertical	Adiabatic
1-pyrazolyl, $\tilde{B}^2B_2$	0.391	0.269	0.380	0.261
1-pyrazolyl, $\tilde{A}^2B_1$	0	0	0.027	0.046
1-pyrazolyl, $\tilde{X}^2A_2$	0.060	0.011	0	0
1-pyrazolide, $\tilde{X}^1A_1$	-2.687	-2.366	-2.976	-2.625
1-imidazolyl, $\tilde{B}^2B_2$	1.299	0.944	1.339	0.958
1-imidazolyl, $\tilde{A}^2A_2$	0.904	0.777	0.990	0.836
1-imidazolyl, $\tilde{X}^2B_1$	0	0	0	0
1-imidazolide, $\tilde{X}^1A_1$	-2.301	-2.047	-2.527	-2.296

method as well as the physical principles underlying it have been well documented;<sup>4</sup> so only a brief description is given below.

It is difficult to treat nonadiabatic interactions in the adiabatic representation because the electronic wave functions are highly sensitive to the nuclear coordinates when degeneracies are nearby. The electronic wave functions can be transformed into the diabatic representation where the nuclear kinetic energy part of the Hamiltonian is approximately diagonal, while the potential energy part becomes nondiagonal. Since the potential energy in the diabatic representation is a smoothly varying function of nuclear coordinates, it can be expanded around a reference geometry where the adiabatic and diabatic potential energies coincide. The adiabatic potential energy surfaces can be obtained by diagonalizing the potential energy matrix.

Thus, our task is to construct model diabatic potentials and to solve the Schrödinger equation defined by the model potentials. The model Hamiltonian in the diabatic representation is given by

$$H = (T_N + V_0) \cdot I + \begin{pmatrix} a & x \\ x & b \end{pmatrix}, \quad (2)$$

where

$$T_N = -\frac{1}{2} \sum_i \omega_i \frac{\partial^2}{\partial q_i^2},$$

$$V_0 = \frac{1}{2} \sum_i \omega_i q_i^2,$$

$$a = E_0^A + \sum_i \kappa_i^A q_i + \frac{1}{2} \sum_{ij} \kappa_{ij}^A q_i q_j,$$

$$b = E_0^B + \sum_i \kappa_i^B q_i + \frac{1}{2} \sum_{ij} \kappa_{ij}^B q_i q_j,$$

$$x = \sum_i \lambda_i q_i.$$

Here,  $T_N$  is the nuclear kinetic energy operator,  $V_0$  is the potential energy of the reference state, and  $I$  is the unit matrix. In the present study, the electronic ground state of the anion is taken as the reference state; i.e., the potential energy is expanded around the equilibrium geometry of the anion ground state. Thus, the natural choice of the nuclear coordinates in the model Hamiltonian is the normal coordinates of the anion ground state. Note that the reduced normal coordinates  $q_i$  are used in the above expressions with the harmonic vibrational frequencies  $\omega_i$ . The expansion of the potential energy is represented by the last matrix in Eq. (2). The diagonal blocks,  $a$  and  $b$ , account for “intrastate coupling” terms taken up to the second order for the neutral states (i.e., radical),  $A$  and  $B$ , respectively. The potential energy of the corresponding state at the reference geometry (i.e., vertical energy) is denoted by  $E_0^{(A \text{ or } B)}$  which is relative to the energy of the reference state. The off-diagonal block  $x$  contains only linear terms that account for “interstate couplings.” For the

sake of simplicity, only two states are considered in the model Hamiltonian in Eq. (2), but extension to a three-state problem is straightforward.

Parametrization of the model potential entails determination of  $E_0$ ,  $\kappa$ , and  $\lambda$ . Since the model potential is expanded around the anion geometry, the  $\kappa$  parameters are the derivatives of the potential energies with respect to the anion reduced normal coordinates at the anion geometry,  $Q_0$ ,

$$\kappa_i^{A,B} = \left( \frac{\partial V^{A,B}}{\partial q_i} \right)_{Q_0}, \quad (3)$$

$$\kappa_{i,j}^{A,B} = \left( \frac{\partial V^{A,B}}{\partial q_i \partial q_j} \right)_{Q_0} - \omega_i \delta_{ij}. \quad (4)$$

The  $\kappa$  so obtained is called the “vertical  $\kappa$ ” in this paper. Symmetry considerations immediately tell that only totally symmetric normal modes have nonzero linear intrastate coupling constants for nondegenerate electronic states. Also, for quadratic coupling constants to be nonzero, the two modes have to belong to the same symmetry.

Evaluation of the derivatives at the reference geometry has been almost exclusively used in the literature to determine  $\kappa$  when the model potential is parametrized by *ab initio* calculations. This method is not only consistent with the underlying physical picture, but is also consistent in a sense with the time-dependent interpretation of spectroscopy which focuses on the short-time dynamics that are necessarily restricted to regions close to the vertical geometry.<sup>4,58–60</sup>

It has been recognized, however, that the model potentials so obtained can conflict with correct vibrational levels around the equilibrium geometries of the corresponding states. Standard FC overlap calculations under the adiabatic approximation take the associated effects of Duschinsky rotation and anharmonicity into account by comparing the normal modes of the initial and final states at the corresponding equilibrium geometries.<sup>38,39</sup> These effects can be treated in the parametrization of the model potentials. Specifically, the mass-weighted quadratic force constant matrix of a particular electronic state of the radical, which is evaluated at its equilibrium geometry, is transformed into a matrix in a basis of the reduced normal coordinates of the anion ground state. Diagonalization of this matrix gives precisely, by construction, the harmonic frequencies and normal modes of the *ab initio* method at the equilibrium geometry of the final (i.e., radical) state. The elements of the resultant matrix  $F$  correspond to the quadratic intrastate coupling constants. This transformed Hessian is multiplied by a vector  $\Delta Q$  representing the displacements of the equilibrium geometries from the anion ground state to the neutral state projected onto the anion reduced normal coordinates. The components of the resultant vector are the linear intrastate coupling constants. In short,

$$\kappa_i^{A,B} = - \sum_j \Delta Q_j \cdot F_{ji}, \quad (5)$$

TABLE III. Linear intrastate coupling constants ( $\kappa_i$  in eV) for the  $\tilde{X}^2A_2$ ,  $\tilde{A}^2B_1$ , and  $\tilde{B}^2B_2$  states of the 1-pyrazolyl- $d_3$  radical, and the  $\tilde{X}^2B_1$ ,  $\tilde{A}^2A_2$ , and  $\tilde{B}^2B_2$  states of the 1-imidazolyl radical, evaluated with EOMIP-CCSD calculations. Both vertical  $\kappa$  and adiabatic  $\kappa$  are shown.

1-pyrazolyl- $d_3$						
	$\tilde{X}^2A_2$		$\tilde{A}^2B_1$		$\tilde{B}^2B_2$	
Mode	Vertical $\kappa$	Adiabatic $\kappa$	Vertical $\kappa$	Adiabatic $\kappa$	Vertical $\kappa$	Adiabatic $\kappa$
1	0.0318	0.0186	0.0548	0.0405	0.0411	0.0290
2	-0.0232	-0.0139	-0.0291	-0.0171	-0.0458	-0.0382
3	0.2023	0.1538	-0.1795	-0.1964	-0.0092	-0.0240
4	-0.2371	-0.2470	0.1796	0.1670	-0.1879	-0.2920
5	0.1234	0.1902	-0.1408	-0.0925	0.2465	0.3549
6	-0.0462	-0.0387	0.0759	0.0793	0.1221	0.1309
7	-0.0017	-0.0240	0.0015	-0.0123	-0.0650	-0.0834
1-imidazolyl						
	$\tilde{X}^2B_1$		$\tilde{A}^2A_2$		$\tilde{B}^2B_2$	
Mode	Vertical $\kappa$	Adiabatic $\kappa$	Vertical $\kappa$	Adiabatic $\kappa$	Vertical $\kappa$	Adiabatic $\kappa$
1	0.0337	0.0258	0.0452	0.0366	0.0582	0.0444
2	0.0164	0.0170	0.0344	0.0348	0.0573	0.0629
3	0.1918	0.1723	-0.1600	-0.1637	-0.0337	-0.0370
4	-0.1711	-0.1791	0.1270	0.1102	-0.0025	0.0041
5	0.0960	0.1342	-0.1670	-0.1251	-0.0790	-0.0599
6	0.0858	0.0649	-0.0861	-0.0993	-0.1457	-0.1564
7	0.0307	0.0287	-0.0853	-0.0822	-0.3068	-0.3154

$$\kappa_{i,j}^{A,B} = F_{ij} - \omega_i \delta_{ij}, \quad (6)$$

where all the quantities have the reduced normal coordinates of the anion ground state as a basis. The set of  $\kappa$  so obtained is called the ‘‘adiabatic  $\kappa$ ’’ in this article. It should be noted that a linear version of Eq. (5) has been used for model potentials of  $\text{NO}_2$  and cyclopentadienyl.<sup>18,61,62</sup> Also, a treatment similar to Eq. (6) has been used in the simulation of the photoelectron spectrum of ethylene.<sup>26</sup> In our implementation, Eq. (6) is used to determine the intrastate quadratic coupling constants only for the totally symmetric modes. However, diagonal quadratic coupling constants for nontotally symmetric modes are included as well in the model potentials, as explained later. The vertical and adiabatic  $\kappa$  are given in Tables III and IV for the 1-pyrazolyl- $d_3$  and 1-imidazolyl systems. Corresponding information for the 1-pyrazolyl- $h_3$  radical is given as supplementary materials.<sup>41</sup>

The same distinction applies to how one can parametrize the vertical energies in the model potentials. It is apparently most obvious to set the vertical energies to coupled-cluster energy calculations of the neutral states at the anion geometry. Table II shows the vertical energies of the neutral states evaluated with EOMIP-CCSD/DZP and CCSD(T)/cc-pVTZ calculations at the anion geometry. The vertical energies so obtained can be combined with the aforementioned vertical  $\kappa$  to construct the model potentials. On the other hand, the vertical energies can also be treated in a way that conforms to the adiabatic  $\kappa$  evaluation. A fundamental idea in the adiabatic  $\kappa$  parametrization is to place emphasis on the potential energy surface around the equilibrium geometry of the final state. In this sense, the potential energy of the neutral state at the corresponding equilibrium geometry (i.e., the adiabatic

energy) is more important for the simulation than that at the anion geometry. Accordingly, the vertical energy can be set to reproduce the adiabatic energy obtained with coupled-cluster calculations within the model potential framework. In other words, the vertical energy is the adiabatic energy of the CCSD(T) calculations plus the energy difference between the anion and neutral equilibrium geometries calculated with the adiabatic  $\kappa$  model potential. It should be mentioned that the solution of the Schrödinger equation depends on the vertical energy difference ( $E_0^A - E_0^B$ ), not on the absolute energy *per se*. The absolute energy in the model potential is set to best fit the final simulated spectrum to the observed one. The lack of diffuse functions in the basis set accounts for most of the discrepancy in the electron affinity between the CCSD(T)/cc-pVTZ calculations and the experimental results (Table II).

The remaining parameters are the linear interstate coupling constants  $\lambda$ , which account for nonadiabatic interactions. Evaluation of the coupling constants is made at the anion geometry, following a standard procedure.<sup>4</sup> Namely, the mass-weighted quadratic force constant matrices of the neutral states, which are calculated at the reference anion geometry, are transformed into the basis of the reduced normal coordinates of the anion ground state. Comparison with the adiabatic potential energies obtained from the model diabatic Hamiltonian provides the relation<sup>11,63</sup>

$$\lambda_i = \sqrt{|\Delta E(f_i^A - f_i^B)|/2}, \quad (7)$$

where  $f_i^A$  and  $f_i^B$  are the diagonal elements of the transformed matrices, and  $\Delta E = E_0^A - E_0^B$  is the energy separation between the two states at the anion geometry. Symmetry considerations dictate that  $\lambda$  is nonzero for normal modes with symmetries such that the direct product with the corresponding

TABLE IV. Quadratic intrastate coupling constants (the adiabatic  $\kappa_{ij}$  in eV) for the  $\tilde{X}^2A_2$ ,  $\tilde{A}^2B_1$ , and  $\tilde{B}^2B_2$  states of the 1-pyrazolyl- $d_3$  radical, and the  $\tilde{X}^2B_1$  state of the 1-imidazolyl radical, evaluated with EOMIP-CCSD calculations. For  $\tilde{X}^2B_1$  1-imidazolyl, the vertical  $\kappa$  are also shown.

1-pyrazolyl- $d_3$ , $\tilde{X}^2A_2$ , adiabatic $\kappa$							
Mode	1	2	3	4	5	6	7
1	0.0161	-0.0001	-0.0053	0.0006	-0.0011	-0.0018	0.0006
2		0.0182	0.0041	-0.0011	-0.0018	-0.0031	-0.0046
3			-0.0132	0.0280	0.0111	0.0043	-0.0004
4				0.0131	-0.0490	-0.0045	0.0171
5					0.0514	0.0028	-0.0095
6						-0.0030	-0.0023
7							0.0056
1-pyrazolyl- $d_3$ , $\tilde{A}^2B_1$ , adiabatic $\kappa$							
	1	2	3	4	5	6	7
1	0.0076	-0.0023	0.0111	0.0021	0.0022	0.0001	-0.0028
2		0.0166	-0.0078	0.0069	-0.0016	-0.0046	0.0068
3			0.0026	-0.0419	-0.0029	-0.0006	-0.0066
4				0.0061	0.0242	-0.0029	-0.0173
5					-0.0354	0.0029	0.0065
6						-0.0030	-0.0005
7							0.0002
1-pyrazolyl- $d_3$ , $\tilde{B}^2B_2$ , adiabatic $\kappa$							
	1	2	3	4	5	6	7
1	0.0153	-0.0051	0.0001	-0.0015	0.0003	-0.0024	0.0063
2		0.0231	0.0033	0.0016	0.0001	-0.0033	-0.0115
3			-0.0193	0.0026	0.0008	0.0101	0.0020
4				0.0640	-0.0631	-0.0012	0.0118
5					0.0690	0.0014	-0.0159
6						-0.0038	0.0015
7							0.0076
1-imidazolyl, $\tilde{X}^2B_1$ , adiabatic $\kappa$							
	1	2	3	4	5	6	7
1	0.0146	0.0009	-0.0113	0.0019	-0.0024	0.0042	-0.0051
2		0.0250	0.0036	-0.0037	-0.0005	-0.0024	-0.0017
3			-0.0229	-0.0110	0.0202	-0.0262	0.0030
4				-0.0008	-0.0285	-0.0004	0.0071
5					0.0271	0.0034	-0.0018
6						-0.0087	-0.0025
7							-0.0022
1-imidazolyl, $\tilde{X}^2B_1$ , vertical $\kappa$							
	1	2	3	4	5	6	7
1	0.0088	-0.0004	0.0030	-0.0003	-0.0018	0.0018	-0.0012
2		0.0110	0.0016	-0.0048	-0.0006	-0.0019	-0.0012
3			0.0133	-0.0061	-0.0025	0.0029	-0.0008
4				0.0000	0.0038	-0.0042	-0.0012
5					-0.0062	-0.0013	-0.0034
6						0.0096	-0.0048
7							0.0029

two neutral states contains the totally symmetric irreducible representation. This derivation of  $\lambda$  implicitly assumes that the quadratic force constants of the two diabatic states are the same. Therefore, the average of the two force constants is

used to derive the intrastate quadratic coupling constant (diagonal) for the corresponding nontotally symmetric modes. The linear interstate coupling constants as well as the diabatic force constants are given in Table V. See the supplement-

TABLE V. Linear interstate coupling constants ( $\lambda_i$  in eV) for the  $\tilde{X}^2A_2$ ,  $\tilde{A}^2B_1$ , and  $\tilde{B}^2B_2$  states of the 1-pyrazolyl- $d_3$  radical, and the  $\tilde{X}^2B_1$ ,  $\tilde{A}^2A_2$ , and  $\tilde{B}^2B_2$  states of the 1-imidazolyl radical evaluated with EOMIP-CCSD calculations. The quadratic force constants (eV) of the diabatic states have also been evaluated at the corresponding anion geometry.

1-pyrazolyl- $d_3$					
$a_2$ mode	$\lambda$ ( ${}^2B_2\text{-}^2B_1$ )	Force constant	$b_2$ mode	$\lambda$ ( ${}^2B_1\text{-}^2A_2$ )	Force constant
8	0.1967	0.0870	13	0.0043	0.3025
9	0.0311	0.0944	14	0.2249	0.1876
$b_1$ mode	$\lambda$ ( ${}^2B_2\text{-}^2A_2$ )				
10	0.0769	0.0968	15	0.0272	0.1618
11	0.0560	0.0592	16	0.1270	0.1194
12	...	0.0896	17	0.0252	0.1173
			18	0.0099	0.0972

1-imidazolyl					
$a_2$ mode	$\lambda$ ( ${}^2B_2\text{-}^2B_1$ )	Force constant	$b_2$ mode	$\lambda$ ( ${}^2A_2\text{-}^2B_1$ )	Force constant
8	0.0298	0.1220	13	...	0.4075
9	0.0544	0.0745	14	0.0819	0.1821
$b_1$ mode	$\lambda$ ( ${}^2B_2\text{-}^2A_2$ )				
10	0.0616	0.1239	15	0.2421	0.1841
11	0.0373	0.1029	16	0.1427	0.1658
12	0.1361	0.0841	17	0.0344	0.1404
			18	0.0760	0.1144

tary materials<sup>41</sup> for the  $\lambda$  parameters for the 1-pyrazolyl- $h_3$  radical.

Now that the model diabatic potentials are defined, the Schrödinger equation is to be solved. The basis functions for the neutral states are

$$|\Phi^{A,l}\rangle = |\psi^A\rangle|\chi^l\rangle, \quad (8)$$

$$|\Phi^{B,m}\rangle = |\psi^B\rangle|\chi^m\rangle,$$

where  $|\psi^{A,B}\rangle$  and  $|\chi^{l,m}\rangle$  represent the electronic and nuclear parts, respectively. It should be noted that the electronic parts include scattering states for the departing photoelectrons in the treatment of photoelectron spectra. Looking at the form of the model Hamiltonian in Eq. (2), it is logical to use the harmonic oscillator eigenfunctions  $|n_i\rangle$  of the anion ground state for the neutral state nuclear basis functions,

$$|\chi^l\rangle = \prod_i |n_i\rangle. \quad (9)$$

Here,  $n_i$  denotes the vibrational quantum number of normal mode  $i$ . Then, the matrix elements of the model Hamiltonian diagonal blocks are obtained in a straightforward manner, viz.,

$$\begin{aligned}
 H_{lm}^{AA,BB} = & \left[ E_0^{A,B} + \sum_i \left( n_i \omega_i + \frac{2n_i + 1}{4} \kappa_{ii}^{A,B} \right) \right] \delta_{lm} \\
 & + \sum_i f_{l,m_i} \kappa_i^{A,B} \prod_{j \neq i} \delta_{l_j, m_j} + \sum_i g_{l,m_i} \kappa_{ii}^{A,B} \prod_{j \neq i} \delta_{l_j, m_j} \\
 & + \sum_{i,j \neq i} h_{l,m_i, l_j, m_j} \kappa_{ij}^{A,B} \prod_{s \neq i,j} \delta_{l_s, m_s}, \quad (10)
 \end{aligned}$$

where

$$f_{l,m_i} = \sqrt{\frac{m_i + 1}{2}} \delta_{l_i, m_i + 1} + \sqrt{\frac{m_i}{2}} \delta_{l_i, m_i - 1},$$

$$g_{l,m_i} = \frac{\sqrt{(m_i + 1)(m_i + 2)}}{4} \delta_{l_i, m_i + 2} + \frac{\sqrt{m_i(m_i - 1)}}{4} \delta_{l_i, m_i - 2},$$

$$\begin{aligned}
 h_{l,m_i, l_j, m_j} = & \frac{\sqrt{(m_i + 1)(m_j + 1)}}{2} \delta_{l_i, m_i + 1} \delta_{l_j, m_j + 1} \\
 & + \frac{\sqrt{(m_i + 1)m_j}}{2} \delta_{l_i, m_i + 1} \delta_{l_j, m_j - 1} \\
 & + \frac{\sqrt{m_i(m_j + 1)}}{2} \delta_{l_i, m_i - 1} \delta_{l_j, m_j + 1} \\
 & + \frac{\sqrt{m_i m_j}}{2} \delta_{l_i, m_i - 1} \delta_{l_j, m_j - 1}.
 \end{aligned}$$

The constant term ( $V_0$ ) is omitted above, since its inclusion acts only to uniformly shift all the eigenvalues. Also, the matrix elements in off-diagonal blocks are

$$H_{lm}^{AB} = \sum_i f_{l,m_i} \lambda_i \prod_{j \neq i} \delta_{l_j, m_j}. \quad (11)$$

The Hamiltonian matrix is sparse, and the Lanczos algorithm is used to transform the matrix into a tridiagonal form, which is then diagonalized.<sup>4</sup> Typically, a thousand Lanczos iterations suffice to give a well-converged spectral profile.

Intensities in the photoelectron spectrum can be expressed as follows:

$$P(E) = \sum_{\alpha,\nu} |\langle \Phi^{\alpha,\nu} | T | \Phi^0 \rangle|^2 \delta(E - E^{\alpha,\nu}). \quad (12)$$

Here,  $T$  is the transition operator and  $E^{\alpha,\nu}$  represents a vibronic energy level belonging to the neutral electronic state  $\alpha$  and the vibrational state  $\nu$ . The wave function of the initial state, i.e., the anion ground state,  $|\Phi^0\rangle$ , is

$$|\Phi^0\rangle = |\psi^0\rangle |\chi^0\rangle. \quad (13)$$

It is obvious that we need to know the transition dipole matrix elements to simulate the spectra. In the diabatic picture, we assume that the transition operator is independent of the nuclear coordinates and all the electronic states of the radical have the same magnitude of the electronic integral of the transition dipole with the anion ground state. At the final stage of simulations, we relax the assumption of identical cross sections to best fit the calculated spectra. It should also be mentioned that the photoelectron kinetic energy dependence of the cross sections is neglected. This approximation appears valid in the range of the photoelectron kinetic energies in our systems, according to the results of the photodetachment cross section measurements reported in the literature for similar molecules.<sup>64,65</sup> As for the nuclear part of the integrals, we consider transitions originating only from the vibrational ground state (zero temperature approximation),

$$|\chi^0\rangle = \prod_i |0_i\rangle. \quad (14)$$

This approximation is particularly good when the ions are synthesized in the flow tube cooled with liquid nitrogen. Therefore, the transition intensities depend on the projection of nuclear wave functions of the neutral states onto the vibrational ground state of the anion. In practice, these quantities are easily retrieved from the Lanczos eigenvectors if an appropriate seed (first trial) vector is used. The transition intensities are convoluted with a Gaussian function to simulate the experimental line shape.

### III. RESULTS

#### A. Electronic structure of the 1-pyrazolyl and 1-imidazolyl radicals

Before investigating nonadiabatic effects in the 1-pyrazolyl radical, we briefly describe its electronic structure in comparison to that of the 1-imidazolyl radical. Figure 1 shows schematic representations of the highest occupied molecular orbitals of the 1-pyrazolide and 1-imidazolide anions. There are significant differences in electronic structure between these two structural isomers, which are associated with different extents of nonadiabatic effects in the corresponding neutral radicals.

The two highest occupied molecular orbitals of the 1-pyrazolide anion, which have  $a_2$  and  $b_1$  symmetries, are almost degenerate. This quasidegeneracy stems from the fact that both orbitals have comparable contributions from the atomic orbitals of the two N atoms. Indeed, they correspond to a degenerate pair of orbitals in the isoelectronic cyclopentadienide anion.<sup>66</sup> Therefore, photodetachment from the two molecular orbitals leads to formation of nearly degenerate

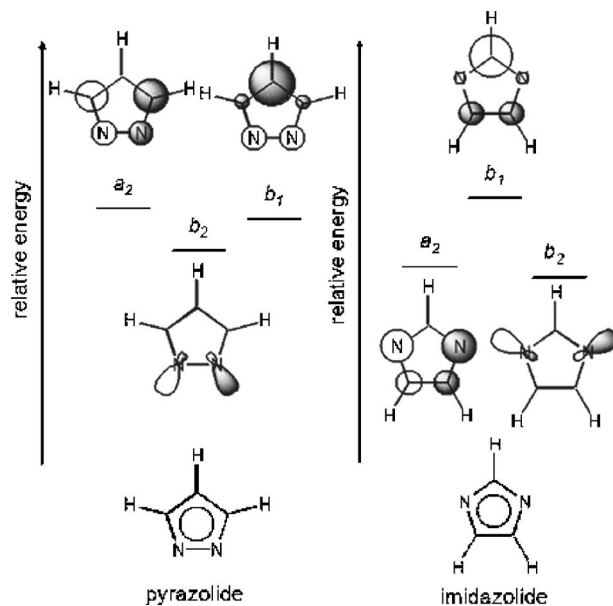


FIG. 1. Schematic representation of the highest occupied molecular orbitals of the 1-pyrazolide anion and the 1-imidazolide anion.

${}^2A_2$  and  ${}^2B_1$  states of the 1-pyrazolyl radical. These two states can have pseudo-Jahn-Teller interactions with each other along  $b_2$  normal coordinates. This near degeneracy may make the nonadiabatic interactions substantial, leading to a complicated vibronic structure in the photoelectron spectrum.

There is another nearby orbital for the 1-pyrazolide anion. Unlike the other two, this orbital, which has  $b_2$  symmetry, is an in-plane molecular orbital, mainly represented by an out-of-phase combination of the two N atom lone-pair orbitals. The repulsive interaction between the two atomic orbitals destabilizes this molecular orbital, such that it approaches the  $a_2$  and  $b_1$  orbitals in energy. This energy destabilization is related to the rather low ionization energy of pyridazine.<sup>67</sup> Photodetachment from this in-plane orbital yields the  ${}^2B_2$  state of the 1-pyrazolyl radical which can interact vibronically with the  ${}^2A_2$  and  ${}^2B_1$  states along  $b_1$  and  $a_2$  normal coordinates, respectively. These additional nonadiabatic interactions may also affect the vibronic structure of the low-lying states.

On the other hand, the highest occupied molecular orbital of the 1-imidazolide anion ( $b_1$  symmetry) is somewhat far above the  $a_2$  orbital in energy. While the  $b_1$  orbital mainly comprises the C atom  $p$  orbitals, the  $a_2$  orbital has major contributions from the N atom  $p$  orbitals. Thus, the  $a_2$  orbital is much more stabilized than the  $b_1$  orbital in the 1-imidazolide anion. The in-plane  $b_2$  molecular orbital is not very close to the  $b_1$  orbital in energy, either, for 1-imidazolide. The difference in the extent of the energy stabilization of the  $b_2$  orbital between the 1-pyrazolide and 1-imidazolide anions is reminiscent of the difference in the ionization energy between pyridazine<sup>67</sup> and pyrimidine.<sup>68</sup> Consequently, nonadiabatic effects in  $\tilde{X}^2B_1$  1-imidazolyl are expected to be much less significant. Simulations of the photoelectron spectrum of the 1-imidazolide anion using the model Hamiltonian are discussed in the next section, so that

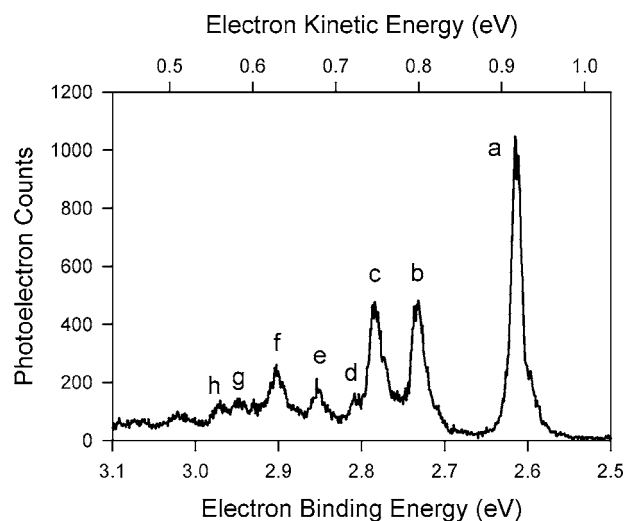


FIG. 2. The 351.1 nm photoelectron spectrum of the 1-imidazolidine anion produced in a flow tube at room temperature. The spectrum was taken at the magic angle.

we can demonstrate the quality of our simulation technique for a system well described by an adiabatic (Franck-Condon) treatment. Also, through simulations of the 1-imidazolidine spectrum, we seek to justify our parametrization method for model potentials.

### B. The photoelectron spectrum of the 1-imidazolidine anion

Figure 2 shows the 351.1 nm magic angle photoelectron spectrum of the 1-imidazolidine anion which has been reported in the literature, where a detailed analysis is given.<sup>2</sup> The spectrum reflects the level structure of the  $\tilde{X}^2B_1$  state of the 1-imidazolyl radical. The laser energy is not high enough to access the  $^2A_2$  and  $^2B_2$  excited states (Table II). The main vibronic features observed in the spectrum have been reproduced reasonably well by FC overlap calculations, under the adiabatic approximation, based on the B3LYP/6-311++G(d,p) optimized geometries and normal modes of  $\tilde{X}^1A_1$  1-imidazolidine and  $\tilde{X}^2B_1$  1-imidazolyl.<sup>2</sup> The most intense peak (peak a) in the spectrum is the vibrational origin of  $\tilde{X}^2B_1$  1-imidazolyl. The other peaks in the spectrum represent the fundamentals, overtones, and combinations of a CC stretching mode and an NC stretching mode. These two totally symmetric modes correspond to  $\nu_6$  and  $\nu_3$  modes obtained with EOMIP-CCSD calculations (see EPAPS<sup>41</sup>). The small shoulder (peak d) has been attributed to the overtone of a  $b_2$  mode as a result of Fermi resonance.<sup>2</sup>

Figure 3 shows our simulations of the 1-imidazolidine spectrum using the model Hamiltonian technique superimposed on the observed spectrum. In both Figs. 3(a) and 3(b), the adiabatic approximation is assumed in the simulations; i.e., only one state, the  $\tilde{X}^2B_1$  state of the 1-imidazolyl radical, is considered in the model Hamiltonian. Only totally symmetric modes are taken into account in the nuclear wave functions because nontotally symmetric modes have negligible contributions to the simulations under the adiabatic approximation.<sup>69</sup> Table VI provides the number of harmonic

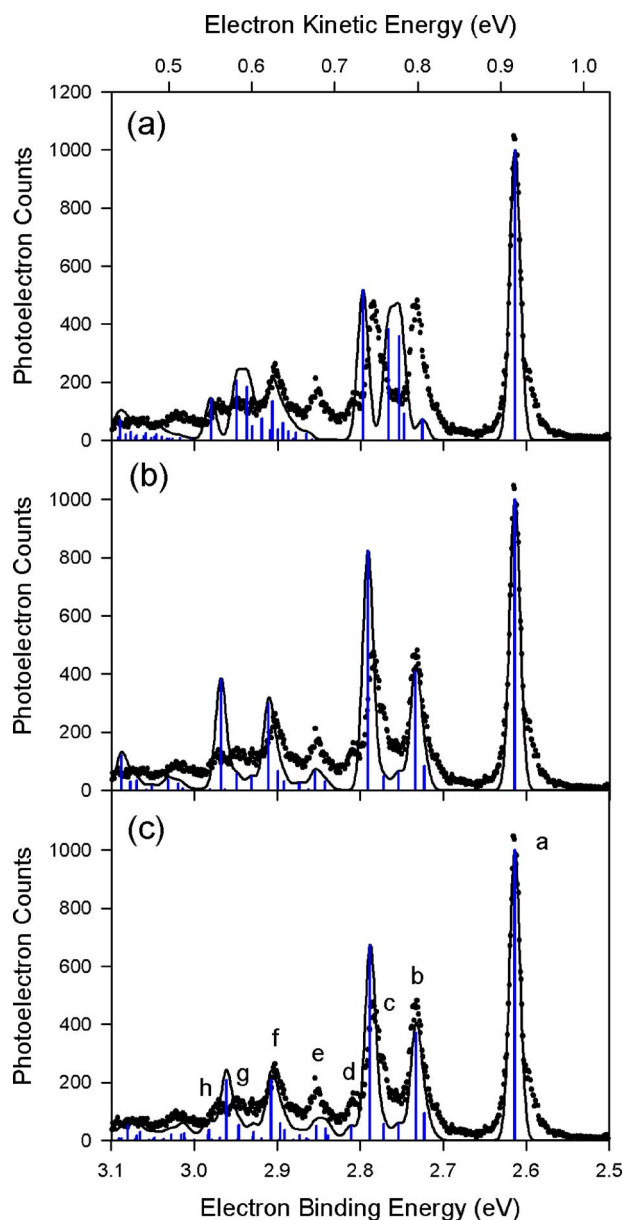


FIG. 3. (Color online) Simulated spectra of the  $\tilde{X}^2B_1$  state of the 1-imidazolyl radical, superimposed on the experimental spectrum (dots). (a) An adiabatic simulation with the vertical  $\kappa$  in the model Hamiltonian. (b) An adiabatic simulation with the adiabatic  $\kappa$  in the model Hamiltonian. (c) A nonadiabatic simulation with the adiabatic  $\kappa$  in the model Hamiltonian that includes the  $\tilde{X}^2B_1$  and  $\tilde{A}^2A_2$  states. The sticks represent the positions and relative intensities of individual vibronic transitions of  $b_1$  (blue) and  $a_2$  (red) symmetries, scaled to the experimental origin peak. The solid lines are the simulated spectra with a Gaussian convolution of a 15 meV full width at half maximum.

oscillator basis functions for each mode used in the calculation. Convergence is reached in the simulations with this size of the nuclear basis; further increase in the basis dimension does not affect the simulated spectral profiles. Among the  $a_1$  modes, the two high-frequency modes, which involve CH stretching motion, are not included. These modes ( $\nu_1$  and  $\nu_2$ ) have negligible effects on the simulations, which is expected from their small linear and quadratic coupling constants (Tables III and IV). The positions and relative intensities of individual vibronic transitions are represented by sticks, and the spectral profile is constructed by convolution with a

TABLE VI. The numbers of harmonic oscillator basis functions for the reduced normal modes of the corresponding anions used in the model Hamiltonian calculations. The total size of the direct product basis is also given.

Mode	Symmetry	1-imidazolyl	1-pyrazolyl- $d_3$
1	$a_1$	1	1
2		1	1
3		9	9
4		7	10
5		10	9
6		6	6
7		7	3
8	$a_2$	1	8
9		1	1
10	$b_1$	1	3
11		1	3
12		1	1
13	$b_2$	1	1
14		4	5
15		4	1
16		4	5
17		1	1
18		4	1
Total basis size		13 547 520	78 732 000

Gaussian function (15 meV full width at half maximum), which is represented by the solid line in the figures.

The difference between the simulations in Figs. 3(a) and 3(b) lies in the way the model Hamiltonian is parametrized. Figure 3(a) shows a simulation with the vertical  $\kappa$  used in the model potential, while the model potential with the adiabatic  $\kappa$  gives a simulated spectrum shown in Fig. 3(b). The peak positions of the fundamentals of the  $\nu_6$  and  $\nu_3$  modes (peaks  $b$  and  $c$ , respectively) are well reproduced when the adiabatic  $\kappa$  is used, even though the intensity of peak  $c$  is somewhat overestimated. Peak positions of the fundamentals in the simulation with the vertical  $\kappa$  are much less satisfactory. Also, the vertical  $\kappa$  simulation predicts three modes with significant fundamental intensities instead of two. These observations are consistent with the way the corresponding intrastate coupling constants are evaluated. For the adiabatic  $\kappa$ , the quadratic coupling constants are derived from the force constant matrix of  $\tilde{X}^2B_1$  1-imidazolyl at its equilibrium geometry, which necessarily provides more correct positions of the vibrational levels of the radical; the positions of the simulated peaks corresponding to peaks  $b$  and  $c$  match the harmonic vibrational frequencies for the  $\nu_6$  and  $\nu_3$  modes, respectively.<sup>41,70</sup> On the other hand, for the vertical  $\kappa$ , the quadratic coupling constants are derived from the force constant matrix of the radical at the anion geometry, where anharmonicity in the true potential gives rise to “shifts” in the harmonic frequencies. The vertical  $\kappa$  are quite different from the adiabatic  $\kappa$ , as seen in Table IV. In light of this comparison, we choose to use the adiabatic  $\kappa$  in the model potentials for spectral simulations. It should be noted that all of the simulations in the present study use the coupling constants shown in Tables III–V, which are *ab initio* values, scaled by 0.95, an empirical factor which improves the correspondence between our simulation and experimental result.<sup>71</sup>

While the prediction of the fundamental peak positions in Fig. 3(b) is satisfactory, the overestimation of the intensity for peak  $c$  compromises the overall quality of the simulation. This problem is carried over to the corresponding combination and overtone peaks. A similar overestimate was observed in our previous adiabatic FC simulation based on the DFT calculations.<sup>2</sup> In this publication, we have noted that the fundamental level of the  $\nu_3$  mode is in Fermi resonance with two quanta of a nontotally symmetric mode, which explains the overestimation of the peak intensity as well as the absence of peak  $d$  in the adiabatic, harmonic FC simulation.<sup>72</sup> We have further discussed the origin of the relatively large anharmonic effect and attributed it to the vibronic interaction between the  $\tilde{X}^2B_1$  and  $\tilde{A}^2A_2$  states.<sup>72</sup>

Figure 3(c) shows a simulation of the spectrum with the vibronic interaction between the two states taken into account. Table VI provides the number of harmonic oscillator basis functions for the vibronic coupling modes, in addition to the  $a_1$  modes, used in the model Hamiltonian. The vertical energies of the two states in the model Hamiltonian are set adiabatically as explained in Sec. II C. The vibronic peaks of  $b_1$  symmetry dominate the spectrum in the energy range shown, while peaks of  $a_2$  symmetry are negligible. With the moderately large energy separation between the  $^2B_1$  and  $^2A_2$  states (Table II) and moderate strengths of the vibronic couplings (Table V), no strong nonadiabatic effects are expected for the  $\tilde{X}^2B_1$  state. However, differences are apparent between the simulations in the presence [Fig. 3(c)] and absence [Fig. 3(b)] of the pseudo-Jahn-Teller interactions. The simulated intensity for peak  $c$  is significantly reduced once the vibronic coupling is taken into account. At the same time, a new peak is predicted right at the higher eBE side of peak  $c$ , as shown in Fig. 3(c), corresponding to peak  $d$ . These observations are consistent with the resonance effects discussed previously.<sup>2,72</sup> Analogous resonance effects are observed for the combination and overtone peaks (peaks  $f$  and  $g$ , respectively) of the  $\nu_3$  mode. Overall, there is significant improvement of the simulation when the vibronic interactions are taken into account. The vibronic interactions with the  $^2B_2$  state do not change the profile of the simulated spectrum for the  $\tilde{X}^2B_1$  state significantly, so these interactions are ignored. The negligible effects from the  $^2B_2$  state are consistent with a rather large energy separation (Table II) and rather small  $\lambda$  (Table V) between the  $^2B_2$  and  $^2B_1$  states.

To summarize our study of the 1-imidazolide spectrum, the vibronic feature of  $\tilde{X}^2B_1$  1-imidazolyl is well reproduced with the model Hamiltonian technique using the adiabatic  $\kappa$ . Inclusion of the  $^2A_2$  state in the Hamiltonian is important with respect to resonance effects on the  $\tilde{X}^2B_1$  spectrum. This study confirms that the model Hamiltonian technique works very well for a system without strong nonadiabatic effects and sets the stage for our study of nonadiabatic effects in the 1-pyrazolyl radical, presented in the next section.

### C. The photoelectron spectrum of the 1-pyrazolide- $d_3$ anion

We have recently reported the photoelectron spectrum of the 1-pyrazolide- $h_3$  anion.<sup>3</sup> The photoelectron angular distri-

butions indicate two nearly degenerate electronic states of the 1-pyrazolyl- $h_3$  radical, separated adiabatically by only  $32 \pm 1$  meV. Our CCSD(T)/cc-pVTZ calculations at the EOMIP-CCSD/DZP optimized geometries support the near degeneracy of the  ${}^2A_2$  and  ${}^2B_1$  states (Table II). It is also noteworthy (Table II) that the calculated vertical energies of the two states are very close to each other, too; i.e., photo-detachment from the 1-pyrazolide anion accesses the immediate vicinity of a conical intersection. In light of the large magnitudes of  $\lambda$  parameters for the  ${}^2A_2$ - ${}^2B_1$  couplings (see EPAPS<sup>41</sup>), substantial nonadiabatic effects in both states are expected, rationalizing why FC simulations under the adiabatic approximation have failed to reproduce the spectrum.<sup>3</sup> Furthermore, another low-lying state,  ${}^2B_2$ , is present (Table II). It vibronically couples with the other two states significantly (see EPAPS<sup>41</sup>).

The nonadiabatic problem in the 1-pyrazolyl radical demands a sizeable basis set for the model Hamiltonian. For comparison, the 1-imidazolide spectrum shown in Fig. 2 is a two-state problem, involving the  ${}^2B_1$  and  ${}^2A_2$  states. Therefore, only  $b_2$  modes need to be considered besides  $a_1$  modes to simulate the  $\tilde{X}{}^2B_1$  spectrum. As a result, the basis dimension required for the 1-imidazolyl problem is only about  $14 \times 10^6$  (Table VI). On the other hand, since three states are energetically very close to each other for 1-pyrazolyl, all modes, i.e.,  $a_1$ ,  $a_2$ ,  $b_1$ , and  $b_2$ , have to be taken into account to simulate the photoelectron spectrum. Such a large dimension of the basis becomes a computational obstacle.

We have computed all the coupling constants for the 1-pyrazolyl- $h_3$  (EPAPS<sup>41</sup>) and 1-pyrazolyl- $d_3$  (Tables III–V) radicals. Because the normal modes are quite different between the two isotopomers, it is not surprising that the coupling constants are quite different as well. We have found that this difference gives the pyrazolyl- $d_3$  system an advantage over the pyrazolyl- $h_3$  system in the model Hamiltonian computation. Consider the  ${}^2A_2$ - ${}^2B_1$  couplings. For the pyrazolyl- $h_3$  system, all  $b_2$  modes, except the high-frequency CH stretching mode ( $\nu_{13}$ ), have coupling constants of significant magnitude (EPAPS<sup>41</sup>). Therefore, five  $b_2$  modes have to be included in the model Hamiltonian to accommodate the vibronic coupling effects. Inclusion of these  $b_2$  modes corresponds to a factor of 1024 (i.e.,  $4^5$ ) in the basis set dimension (EPAPS<sup>41</sup>). In contrast, the vibronic coupling effects are virtually condensed into only two  $b_2$  modes,  $\nu_{14}$  and  $\nu_{16}$ , in the pyrazolyl- $d_3$  system (Table V). As a result, a factor of 25 (five functions per mode) in the basis set is enough to take care of the  ${}^2A_2$ - ${}^2B_1$  couplings (Table VI).<sup>73</sup> This reduction in the size of the model Hamiltonian leads to the possibility that the full, three-state vibronic interactions in the pyrazolyl- $d_3$  radical can be studied. The size of the basis set used for the full, three-state simulation of the pyrazolyl- $d_3$  system is about  $80 \times 10^6$  (Table VI). The difference in the vibronic coupling scheme between the 1-pyrazolyl isotopomers is somewhat reminiscent of the cyclopentadienyl system.<sup>61,62</sup>

Figure 4(a) shows the photoelectron spectrum of the 1-pyrazolide- $d_3$  anion measured at the magic angle. Measurements have been made at different  $\theta$  [see Eq. (1)], and the spectra taken at the magic angle,  $\theta=0$ , and  $\theta=90^\circ$  are

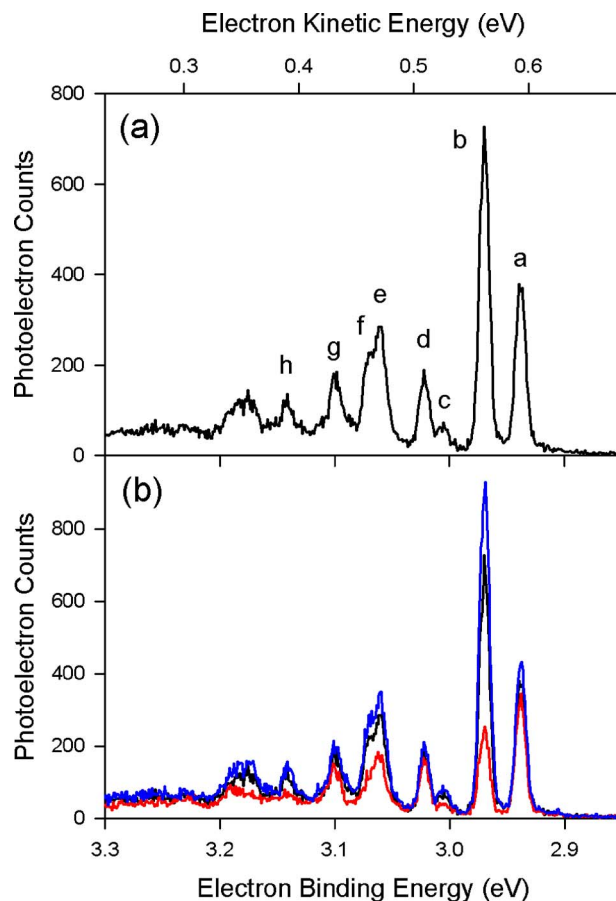


FIG. 4. (Color online) The 351.1 nm photoelectron spectra of the 1-pyrazolide- $d_3$  anion produced in a flow tube cooled with liquid nitrogen. (a) A spectrum taken at the magic angle. (b) Spectra taken at  $\theta=54.7^\circ$  (black),  $0^\circ$  (red), and  $90^\circ$  (blue).

displayed in Fig. 4(b). The anisotropy parameters  $\beta$  have been determined for each peak and reported in Table VII together with the observed peak positions.

The observed spectrum has resemblance to the spectrum of the 1-pyrazolide- $h_3$  anion reported previously<sup>3</sup> (and also presented as supplementary materials of this article<sup>41</sup>). The most intense peaks, peaks *a* and *b*, are separated by only  $32 \pm 1$  meV, with quite different  $\beta$  values, indicating the presence of two nearly degenerate states of the 1-pyrazolyl-

TABLE VII. The positions (eV) and  $\beta$  values of the peaks observed in the photoelectron spectrum of the 1-pyrazolide- $d_3$  anion. Peak labels correspond to those in Fig. 4. The uncertainties in the  $\beta$  values are  $\pm 0.1$ .

1-pyrazolyl- $d_3$				
Peak	Position <sup>a</sup>	Position <sup>b</sup>	$\beta$	Assignment
<i>a</i>	0	$-0.032 \pm 0.001$	-0.20	Origin, ${}^2A_2$
<i>b</i>	$0.032 \pm 0.001$	0	-0.65	Origin, ${}^2B_1$
<i>c</i>	$0.067 \pm 0.002$	$0.035 \pm 0.002$	-0.40	...
<i>d</i>	$0.084 \pm 0.002$	$0.052 \pm 0.001$	-0.20	1 quantum, $b_2$ , ${}^2B_1$
<i>e</i>	$0.122 \pm 0.002$	$0.091 \pm 0.002$	-0.40	...
<i>f</i>	$0.133 \pm 0.003$	$0.102 \pm 0.003$	-0.50	...
<i>g</i>	$0.162 \pm 0.003$	$0.130 \pm 0.002$	-0.25	1 quantum, $\nu_4$ , ${}^2A_2$
<i>h</i>	$0.203 \pm 0.003$	$0.171 \pm 0.003$	-0.45	1 quantum, $\nu_3$ , ${}^2B_1$

<sup>a</sup>Relative to peak *a*.

<sup>b</sup>Relative to peak *b*.

$d_3$  radical. According to the coupled-cluster calculations (Table II), which predict the near degeneracy of the  ${}^2A_2$  and  ${}^2B_1$  states, the  ${}^2B_2$  state lies adiabatically 0.26 eV above the ground state (with harmonic zero-point energy correction). With peak *a* assigned as the origin of the ground state, the  ${}^2B_2$  state is expected to be accessible in our experiment, according to the calculations. The observed spectrum, however, appears to exhibit no clear sign of the  ${}^2B_2$  state.

We have attempted to simulate the spectrum with the model Hamiltonian that includes the  ${}^2A_2$ ,  ${}^2B_1$ , and  ${}^2B_2$  states. As explained in Sec. III B, the adiabatic  $\kappa$  is used in the model potentials. As will be demonstrated, the observed spectrum is well reproduced by the simulation, where all vibronic interactions within each pair of the three states are important. In order to dissect the intricate mechanism of the nonadiabatic interactions among the three states, we have performed simulations of the three states with varying treatments of the vibronic interactions. Below, we present our simulations with the one-state model Hamiltonians (i.e., the adiabatic simulations), the two-state ( ${}^2A_2$ - ${}^2B_1$ ) model Hamiltonian, and the three-state model Hamiltonian.

Figure 5 shows model Hamiltonian simulations of the  ${}^2A_2$ ,  ${}^2B_1$ , and  ${}^2B_2$  states under the adiabatic assumption. The sticks indicate the positions and relative intensities of individual vibronic transitions, and the solid lines are the results of the Gaussian convolution with a 10 meV full width at half maximum. As in the case of the adiabatic simulation for the 1-imidazolyl system, only totally symmetric modes are included in the model Hamiltonian, with two high-frequency CD stretching modes excluded. Convergence is reached in the simulations with the number of harmonic oscillator basis functions displayed in Table VI. In the  ${}^2A_2$  spectrum [Fig. 5(a)], five sticks next to the origin peak represent transitions to the fundamental levels of the five  $a_1$  modes of the  ${}^2A_2$  1-pyrazolyl- $d_3$ . Due to the adiabatic  $\kappa$  in the model Hamiltonian, the positions of these fundamental levels match the EOMIP-CCSD harmonic vibrational frequencies of the  ${}^2A_2$  state (Table I). Among the five  $a_1$  modes, the fundamental peak of the  $\nu_4$  mode has the largest intensity, comparable to that of the origin peak. This mode represents CC symmetric stretch and NN stretch motion. The  $\nu_5$  fundamental peak also has large intensity. This mode corresponds to CN stretch and CC symmetric stretch. All the other vibronic peaks at higher eBE are combinations and overtones of the five  $a_1$  modes.

The origin peak of the  ${}^2B_1$  spectrum, shown in Fig. 5(b), is located higher in energy than that of the  ${}^2A_2$  spectrum (see Table VIII for the vertical energy of the  ${}^2B_1$  state relative to that of the  ${}^2A_2$  state used in the simulation). Three vibronic transitions next to the origin peak represent the fundamental levels of the  $\nu_7$ ,  $\nu_6$ , and  $\nu_5$  modes. Among them, the  $\nu_6$  and  $\nu_5$  transitions have larger intensities, but the positions of the transitions are very close to each other, so the two transitions are not resolved when a width of 10 meV is used. The  $\nu_6$  mode represents CCC bend and CCN bend, while NN stretching and CCC bending motion are involved in the  $\nu_5$  mode. The  $\nu_4$  mode has negligible intensity according to the simulation, so that transition to the fundamental level is not visible in the spectrum. On the other hand, the  $\nu_3$  mode has

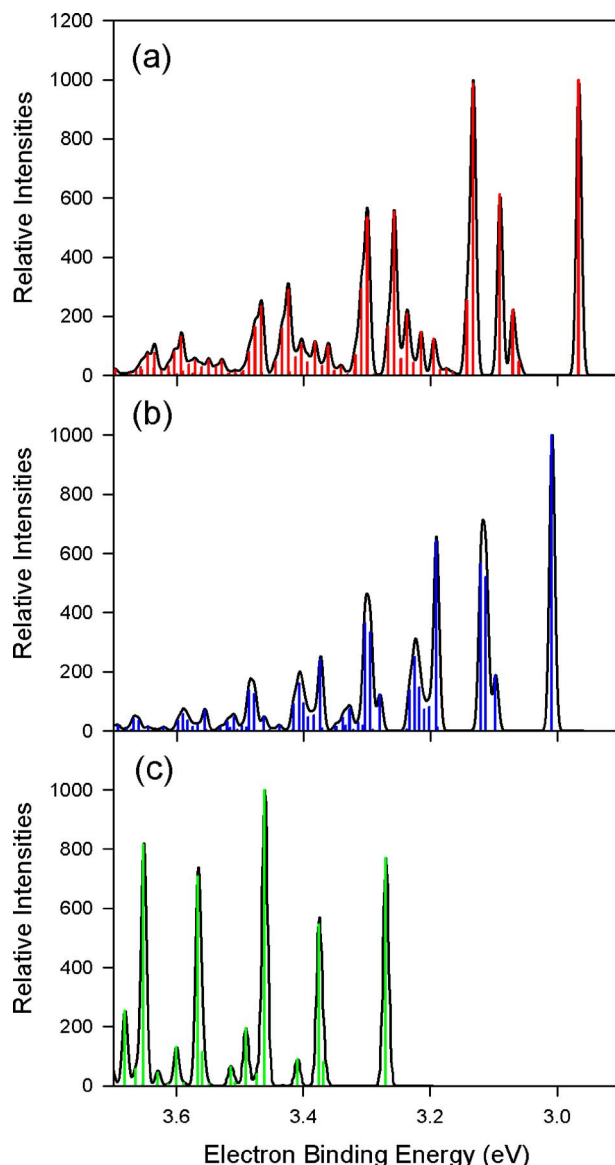


FIG. 5. (Color online) Adiabatic simulations of the spectra of the (a)  $\tilde{X}^2A_2$ , (b)  $\tilde{A}^2B_1$ , and (c)  $\tilde{B}^2B_2$  states of the 1-pyrazolyl- $d_3$  radical with the adiabatic  $\kappa$  in the model Hamiltonian. The sticks represent the positions and relative intensities of individual vibronic transitions. The solid lines are the simulated spectra with a Gaussian convolution of a 10 meV full width at half maximum.

the largest intensity among the transitions to the fundamental levels of the  $a_1$  modes. This mode corresponds to a mixture of CN stretch and CCC bend.

Figure 5(c) shows the simulation of the  ${}^2B_2$  spectrum. The most intense peak appears at eBE of  $\sim 3.46$  eV, which is the transition to the fundamental level of the  $\nu_3$  mode. An extensive vibrational progression of this NN stretch mode is predicted in the simulation, although peaks of up to only two quanta are shown in the energy scale of Fig. 5(c). The  $\nu_6$  mode, which represents CCC bending and CCN bending motion, is also quite active in the simulated spectrum. The transitions to the vibrational levels of the  $\nu_7$  and  $\nu_5$  modes are rather weak, while that of the  $\nu_4$  mode is negligible.<sup>74</sup>

In Fig. 6, the adiabatic simulations of the  ${}^2A_2$  and  ${}^2B_1$  states are superimposed on the observed spectrum. Here, the

TABLE VIII. Summary of the model potential information on the  $C_{2v}$  stationary points,  $C_s$  saddle point, and minimum-energy conical intersections (CI) for the 1-pyrazolyl- $d_3$  radical. Geometry parameters are given in terms of the reduced normal coordinates of the 1-pyrazolide- $d_3$  anion. [The corresponding *ab initio* values are given in parentheses. Geometries have been optimized with EOMIP-CCSD/DZP, and the energies have been calculated with CCSD(T)/cc-pVTZ.]

	Pyrazolide				Pyrazolyl			
	$\tilde{X}^1A_1$	$\tilde{X}^2A_2$	$\tilde{A}^2B_1$	$\tilde{B}^2B_2$	Saddle point	CI ( $^2A_2$ - $^2B_1$ )	CI ( $^2B_2$ - $^2B_1$ )	CI ( $^2B_2$ - $^2A_2$ )
Vertical energy	0	3.270	3.255	3.692	...	...	...	...
Adiabatic energy	0	2.944	3.004	3.231	3.072	3.246	3.319	3.234
(Relative to $^2A_2$ )	-2.944	0	0.060	0.287	0.128	0.302	0.375	0.290
		(0)	(0.060)	(0.287)	(0.133)	(0.335)	(0.436)	(0.292)
Geometry								
$a_1$ mode								
1	0	-0.080	-0.164	-0.104	(-0.132)	-0.100 (-0.113)	-0.123 (-0.125)	-0.099 (-0.100)
2	0	0.066	0.096	0.119	(0.073)	0.045 (0.067)	0.080 (0.096)	0.113 (0.112)
3	0	-1.163	0.858	0.208	(-0.059)	0.220 (-0.045)	0.664 (0.525)	0.102 (0.023)
4	0	1.559	-1.060	0.912	(0.264)	0.133 (0.215)	0.401 (0.335)	0.937 (0.977)
5	0	-0.538	1.189	-1.377	(0.224)	-0.252 (0.099)	-0.871 (-0.671)	-1.325 (-1.275)
6	0	0.481	-0.783	-1.213	(-0.151)	-0.218 (-0.149)	-1.012 (-1.031)	-1.070 (-0.987)
7	0	-0.066	-0.098	0.514	(0.028)	0.179 (0.012)	0.485 (0.374)	0.472 (0.451)
$b_2$ mode								
13	0	0	0	0	(0.010)	0	0	0
14	0	0	0	0	(1.249)	0	0	0
15	0	0	0	0	(-0.213)	0	0	0
16	0	0	0	0	(-1.080)	0	0	0
17	0	0	0	0	(-0.212)	0	0	0
18	0	0	0	0	(-0.078)	0	0	0

positions and intensities of the  $^2A_2$  and  $^2B_1$  simulations are adjusted to match those of peaks *a* and *b*, respectively. We will demonstrate later that peaks *a* and *b* are the origins of the  $^2A_2$  and  $^2B_1$  states, respectively, when we discuss the final, three-state simulation. The solid line in the figure is the Gaussian convolution of vibronic transitions to both states [full width at half maximum (FWHM)=10 meV]. This summation of the adiabatic simulations provides an extremely unfaithful representation of the observed spectrum. Peaks *c* and *d* are completely missed in the simulation. Addition of the adiabatic simulation of the  $^2B_2$  state will not remedy this failure because the calculated adiabatic energy of this state is much higher (Table II). There are several vibronic transitions with considerable intensities predicted in the region of peaks *e* and *f*, but the overall shape of the simulated peaks does not match the observed peaks well. At the higher eBE, the intensities of several peaks are grossly overestimated. Thus, this figure displays the inadequacy of the adiabatic treatment, as in the case of the pyrazolyl- $h_3$  system discussed before.<sup>3</sup>

Next, we study how vibronic coupling between the  $^2A_2$  and  $^2B_1$  states affects the spectrum. Figure 7(a) shows the

results of the simulation where the two states are vibronically coupled. Convergence of the simulation is achieved effectively with the number of harmonic oscillator basis functions shown in Table VI for the additional  $b_2$  modes. In order to demonstrate the nonadiabatic effects, the adiabatic simulations for the two states from Fig. 5 are compared with the nonadiabatic simulation (dashed line) in Figs. 7(b) and 7(c). The positions and intensities of the adiabatic spectra are adjusted such that the corresponding origin peaks match each other. A peak at eBE =  $\sim$  3.03 eV with considerable intensity in Fig. 7(a) has an  $a_2$  symmetry. There is no peak of comparable intensity in this energy region in the adiabatic simulation of the  $^2A_2$  state. This peak arises from nonadiabatic interactions of the  $^2A_2$  and  $^2B_1$  states. In other words, this peak represents the fundamental vibrational level of a  $b_2$  mode of the  $^2B_1$  state, while its intensity originates from the transition dipole moment of the  $^2A_2$  state. The most intense peak of  $a_2$  symmetry, besides the origin peak, in the nonadiabatic simulation (at eBE =  $\sim$  3.12 eV) seems to correspond to the fundamental level of the  $\nu_4$  mode of the  $^2A_2$  state. Its vibrational energy is slightly shifted upwards and its relative intensity is

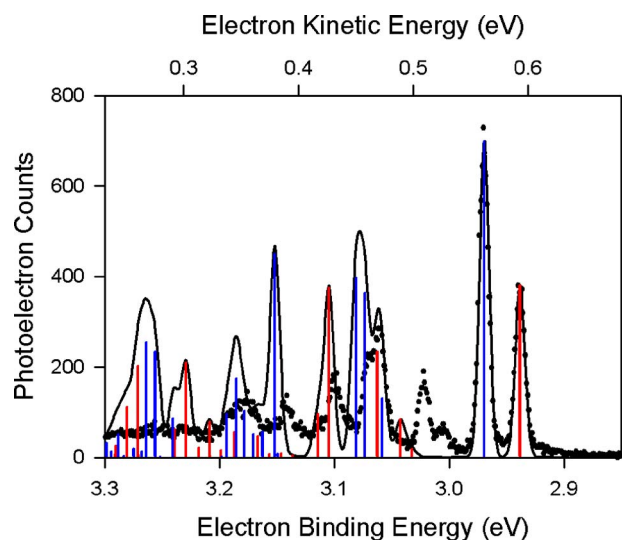


FIG. 6. (Color online) Adiabatic simulations of the spectra of the  $\tilde{X}^2A_2$  and  $\tilde{A}^2B_1$  states of the 1-pyrazolyl- $d_3$  radical with the adiabatic  $\kappa$  in the model Hamiltonian, superimposed on the experimental spectrum (dots). The sticks represent the positions and relative intensities of individual vibronic transitions of  $a_2$  (red) and  $b_1$  (blue) symmetries, scaled to the corresponding origin peaks observed in the experiment. The solid line is the simulated spectrum with a Gaussian convolution of a 10 meV full width at half maximum.

significantly reduced due to the nonadiabatic interactions. Analogously, the relative intensity of the fundamental peak of the  $\nu_5$  mode of the  $^2A_2$  state (at eBE =  $\sim 3.07$  eV) is considerably diminished when the nonadiabatic interactions are included. It is noticeable that the overtone and combination peaks of the  $a_1$  modes are affected substantially by the nonadiabatic interactions as well.

A huge impact of the nonadiabatic interactions is also apparent on the vibronic transitions of  $b_1$  symmetry. While the transitions to the fundamental levels of the  $\nu_6$ ,  $\nu_5$ , and  $\nu_3$  modes have large intensities in the adiabatic simulation of the  $^2B_1$  state, these peaks are all diminished considerably, in addition to exhibiting slight energy shifts, in the nonadiabatic simulation. On the other hand, the fundamental peak of the  $\nu_7$  mode appears to gain intensity through the nonadiabatic interactions, as its energy level shifted downwards. Another feature in the nonadiabatic simulation is a large number of peaks of small intensities, both of  $a_2$  and  $b_1$  symmetries, particularly at higher eBE.

The two-state nonadiabatic simulation is compared to the experimental spectrum in Fig. 8. Note that this nonadiabatic simulation reflects the vertical energy parameters shown in Table VIII, unlike Fig. 6 where the peak positions and intensities of the two adiabatic simulations are scaled to the corresponding origins. The simulated spectrum in Fig. 8 exhibits significant improvements on the adiabatic simulation in Fig. 6. For instance, the nonadiabatic simulation finds peak *d* to be the fundamental level of a  $b_2$  mode of the  $^2B_1$  state. The position of peak *d* is well reproduced, considering the energy offset of the  $^2B_1$  origin peak. The  $\beta$  value of peak *d* is  $-0.20$  (Table VII). This value is significantly different from that of the  $^2B_1$  origin peak (peak *b*),  $-0.65$ . This difference is consistent with the results of the nonadiabatic simu-

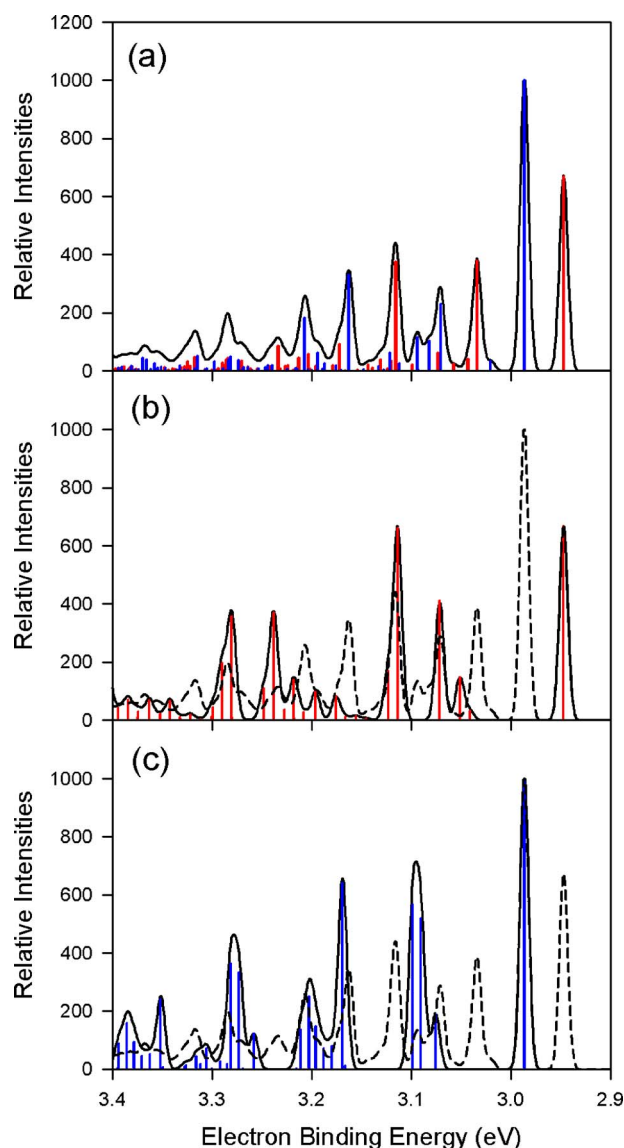


FIG. 7. (Color online) A nonadiabatic simulation with the adiabatic  $\kappa$  in the model Hamiltonian that includes the  $\tilde{X}^2A_2$  and  $\tilde{A}^2B_1$  states of the 1-pyrazolyl- $d_3$  radical. (a) The sticks represent the positions and relative intensities of individual vibronic transitions of  $a_2$  (red) and  $b_1$  (blue) symmetries. The solid line is the simulated spectrum with a Gaussian convolution of a 10 meV full width at half maximum. (b) An adiabatic simulation of the  $\tilde{X}^2A_2$  spectrum from Fig. 5(a) (solid line), superimposed on the two-state nonadiabatic simulation (dashed line). (c) An adiabatic simulation of the  $\tilde{A}^2B_1$  spectrum from Fig. 5(b) (solid line), superimposed on the two-state nonadiabatic simulation (dashed line).

lation which predicts  $a_2$  and  $b_1$  vibronic symmetries for peaks *d* and *b*, respectively. Indeed, peak *a*, which represents the  $^2A_2$  origin, has a  $\beta$  value of  $-0.20$ , just like peak *d*.

The correspondence of the nonadiabatic simulation to the other peaks in the observed spectrum is also much better than that of the adiabatic simulations. Particularly, the intensities of many peaks are reduced by the nonadiabatic interactions, improving the match between the simulation and the observed spectrum. Also, the relative intensities of the two origin peaks in the simulation are in good agreement with those in the observed spectrum. However, for the other observed main peaks, the two-state nonadiabatic simulation

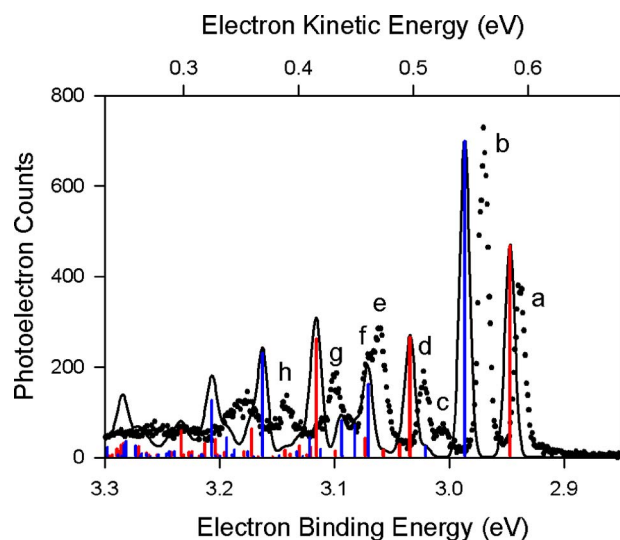


FIG. 8. (Color online) A nonadiabatic simulation with the adiabatic  $\kappa$  in the model Hamiltonian that includes the  $\tilde{X}^2A_2$  and  $\tilde{A}^2B_1$  states of the 1-pyrazolyl- $d_3$  radical, superimposed on the experimental spectrum (dots). The sticks represent the positions and relative intensities of individual vibronic transitions of  $a_2$  (red) and  $b_1$  (blue) symmetries. The solid line is the simulated spectrum with a Gaussian convolution of a 10 meV full width at half maximum.

does not reproduce the relative intensities very well, and the agreement of peak positions is certainly not perfect.

The effects of couplings with the  ${}^2B_2$  state are studied next. Figure 9(a) shows the results of a simulation where the pairs of the  ${}^2A_2$ - ${}^2B_1$  states and the  ${}^2B_2$ - ${}^2B_1$  states are vibronically coupled, but no vibronic interactions are included for the  ${}^2B_2$ - ${}^2A_2$  pair in the model Hamiltonian. The couplings between the  ${}^2B_2$  and  ${}^2B_1$  states result in lowering of the vibronic levels belonging to the  ${}^2B_1$  state relative to the  ${}^2A_2$  state. Thus, the energy separation between the  ${}^2A_2$  and  ${}^2B_1$  origin peaks is reduced by the  ${}^2B_2$ - ${}^2B_1$  coupling. However, the effects of the  ${}^2B_2$ - ${}^2B_1$  interactions are not limited to merely energy shifts of the peaks relative to those simulated with the two-state model Hamiltonian. Relative intensities of the peaks in the two-state simulation [Fig. 7(a) or 8] are also perturbed as a result of the  ${}^2B_2$ - ${}^2B_1$  interactions. In the three-state simulation, a peak of  $b_1$  symmetry in the region of peaks *e* and *f* becomes the most intense besides the origin peaks. Also noticeable is the appearance of a small peak of  $b_2$  symmetry in the region of peak *c*. This peak must represent the fundamental level of an  $a_2$  mode of the  ${}^2B_1$  state. Meanwhile, the three-state simulation does not exhibit any distinct peak of the  ${}^2B_2$  origin, in contrast to the adiabatic simulation [Fig. 5(c)]. Instead, there are a large number of peaks of  $b_2$  symmetry with small intensities in the higher eBE region of the simulated spectrum. The vibrational levels of the  ${}^2B_2$  state find themselves in the midst of a great number of dense vibrational levels of the  ${}^2B_1$  state, and the transition intensities are spread over numerous vibronic levels as a result of the strong vibronic coupling between the  ${}^2B_2$  and  ${}^2B_1$  states.

The simulation in Fig. 9(b) uses the model Hamiltonian where the  ${}^2B_2$ - ${}^2B_1$  vibronic interactions are turned off while each pair of the  ${}^2A_2$ - ${}^2B_1$  states and  ${}^2B_2$ - ${}^2A_2$  states is vibroni-

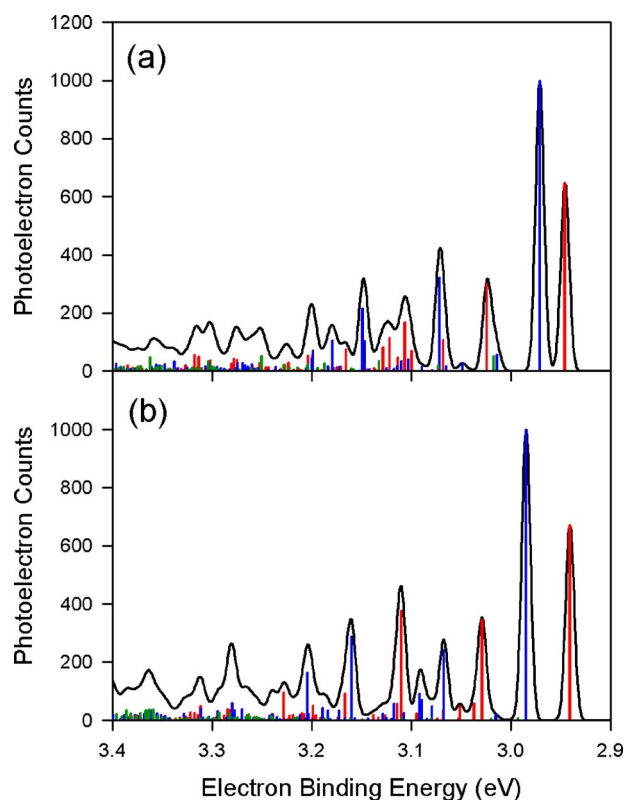


FIG. 9. (Color online) Nonadiabatic simulations with the adiabatic  $\kappa$  in the model Hamiltonian that includes the  $\tilde{X}^2A_2$ ,  $\tilde{A}^2B_1$ , and  $\tilde{B}^2B_2$  states of the 1-pyrazolyl- $d_3$  radical, which are partially coupled. (a) the  ${}^2A_2$ - ${}^2B_1$  couplings and the  ${}^2B_2$ - ${}^2B_1$  couplings are taken into account in the Hamiltonian. (b) the  ${}^2A_2$ - ${}^2B_1$  couplings and the  ${}^2B_2$ - ${}^2A_2$  couplings are taken into account in the Hamiltonian. The sticks represent the positions and relative intensities of individual vibronic transitions of  $a_2$  (red),  $b_1$  (blue), and  $b_2$  (green) symmetries. The solid lines are the simulated spectra with a Gaussian convolution of a 10 meV full width at half maximum.

cally coupled. Analogous to the situation for the  ${}^2B_2$ - ${}^2B_1$  couplings discussed above, the  ${}^2B_2$ - ${}^2A_2$  interactions push down the vibrational levels of the  ${}^2A_2$  state relative to the  ${}^2B_1$  state, but the magnitudes of the energy shifts of the main  ${}^2A_2$  peaks are not as large as those observed for the  ${}^2B_2$ - ${}^2B_1$  interactions. Also, a comparison of the three-state simulation and the two-state simulation [Fig. 7(a)] reveals that the overall spectral profile is not much affected by the  ${}^2B_2$ - ${}^2A_2$  couplings. These observations are consistent with the fact that the interstate coupling for the  ${}^2B_2$ - ${}^2A_2$  pair is not as strong as that for the  ${}^2B_2$ - ${}^2B_1$  pair (Table V).

Finally, Fig. 10(a) shows a simulation of the photoelectron spectrum of the 1-pyrazolide- $d_3$  anion, where all vibronic couplings among the  ${}^2A_2$ ,  ${}^2B_1$ , and  ${}^2B_2$  states are included in the model Hamiltonian. This simulation is superimposed on the observed spectrum in Fig. 10(b). While equal magnitudes of the transition dipole integrals are assumed for the three states in Fig. 10(a), that for the  ${}^2A_2$  state is scaled by a factor of 0.92 in the simulation in Fig. 10(b) such that the relative intensities of the  ${}^2A_2$  and  ${}^2B_1$  origin peaks in the simulation match those observed experimentally. The overall quality of this three-state simulation is striking and represents a further improvement on the two-state simulation shown in Fig. 8.

The success of the nonadiabatic simulation confirms that

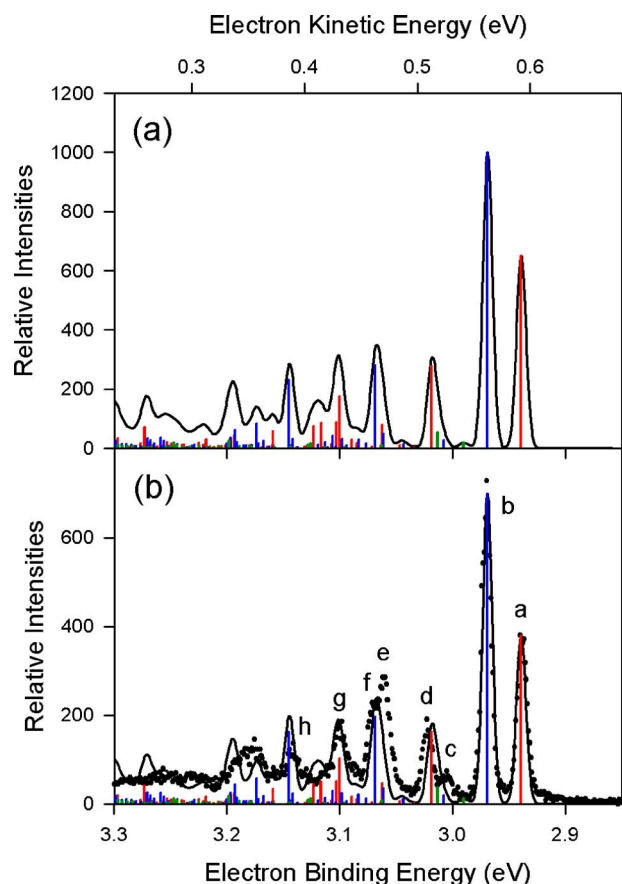


FIG. 10. (Color online) A nonadiabatic simulation with the adiabatic  $\kappa$  in the model Hamiltonian that includes the  $\tilde{X}^2A_2$ ,  $\tilde{A}^2B_1$ , and  $\tilde{B}^2B_2$  states of the 1-pyrazolyl-*d*<sub>3</sub> radical, which are fully coupled. (a) The sticks represent the positions and relative intensities of individual vibronic transitions of  $a_2$  (red),  $b_1$  (blue), and  $b_2$  (green) symmetries. The solid line is the simulated spectra with a Gaussian convolution of a 10 meV full width at half maximum. (b) The simulated spectrum superimposed on the experimental spectrum (dots). The magnitude of the transition dipole moment for the  $\tilde{X}^2A_2$  state has been scaled down by a factor of 0.92 in this simulation to match the relative intensities of the origin peaks for the  $\tilde{X}^2A_2$  and  $\tilde{A}^2B_1$  states to those observed experimentally.

peaks *a* and *b* represent the origins of the  $^2A_2$  and  $^2B_1$  states, respectively. These assignments are consistent with the distinct  $\beta$  values observed for these two peaks (Table VII). The fully coupled three-state simulation gives an energy separation between the  $\tilde{X}^2A_2$  and  $\tilde{A}^2B_1$  origin peaks of 30 meV, in remarkable agreement with the experimental value of  $32 \pm 1$  meV. Notice the decrease in the energy separation from 39 meV predicted in the two-state simulation (Fig. 8). This decrease is a manifestation of the stronger vibronic interactions between the  $\tilde{B}^2B_2$  and  $\tilde{A}^2B_1$  states than those between the  $\tilde{B}^2B_2$  and  $\tilde{X}^2A_2$  states. The electron affinity of the 1-pyrazolyl-*d*<sub>3</sub> radical is  $2.935 \pm 0.006$  eV.

The assignment of peak *c* remains uncertain. According to the simulation, there seem to be two candidates. One is the fundamental level of a  $b_2$  mode of the  $\tilde{X}^2A_2$  state. This peak of  $b_1$  symmetry in the simulation appears closest to peak *c* energywise, but the relative intensity is predicted to be quite small. The other candidate is the fundamental level of an  $a_2$  mode of the  $\tilde{A}^2B_1$  state. The position of this peak of  $b_2$

symmetry is off that of peak *c* to the higher energy side, but the intensity seems to match that of peak *c* very well. It is appropriate to point out that the parameters for these vibronic coupling modes in the model Hamiltonian have been evaluated at the vertical position. Therefore, these parameters are not expected to lead to correct positions of the vibrational levels for the nontotally symmetric modes, which are quantities associated with the potential energy surface around the equilibrium geometry. It is relevant to consider the  $\beta$  value of peak *c* in the discussion of the assignment. If peak *c* has a  $b_1$  symmetry, then the observed  $\beta$  value should be similar to that of peak *b*, the  $^2B_1$  origin, which is indeed the case (Table VII). Unfortunately, in the absence of any distinct peaks of  $b_2$  symmetry in the spectrum (see below), this information cannot be used to assess the assignment of peak *c* as a  $b_2$  symmetry. It should be mentioned that photoelectrons detached from in-plane molecular orbitals localized on a C atom of aromatic anions tend to have positive  $\beta$  values at low kinetic energies.<sup>3,75</sup> The  $b_2$  molecular orbitals are also in-plane orbitals, but the highest occupied molecular orbital of  $b_2$  symmetry in the anion is composed mainly of an out-of-phase combination of the lone-pair orbitals of the two adjacent N atoms. Photoelectrons detached from such a  $b_2$  orbital may have negative  $\beta$  values in the low kinetic energy region. It has been known that detachment from bonding and antibonding combinations of *s* orbitals gives photoelectrons with quite different angular distributions in the coinage metal dimers.<sup>76,77</sup> Thus, peak *c* could be assigned to be either of the two levels, or a mixture of both.

Peak *d* is assigned to be the fundamental level of a  $b_2$  mode of the  $\tilde{A}^2B_1$  state, following the analysis of the two-state simulation (Fig. 8). This assignment conforms to the observed photoelectron angular distributions as discussed earlier.

As for the eBE region near peaks *e* and *f*, the simulation predicts a rather intense peak of  $b_1$  symmetry. Experimentally, peak *e* has a shoulder to the higher eBE side, which is labeled as peak *f*. When two Gaussian peaks are assumed to represent this profile, the energy separation of the two peaks is only 11 meV (Table VII). This feature of the band is not precisely reproduced by the simulation. To the lower eBE side of the intense  $b_1$  vibronic transition, however, the simulation predicts two, almost coincident vibronic transitions with significant intensities, one of which is  $a_2$  symmetry and the other is  $b_1$  symmetry. The contributions from these two vibronic transitions may constitute peak *e*, although its intensity is severely underestimated. Then, the intense  $b_1$  peak in the simulation corresponds to peak *f*. At least, these assignments do not contradict the observed  $\beta$  values. The  $\beta$  values of both peaks are quite negative, analogous to peak *b*, indicating a  $b_1$  character. Also, the fact that the  $\beta$  value of peak *e* is less negative than that of peak *f* may reflect a partial contribution from  $a_2$  transition to peak *e*. As compared with the adiabatic simulation and the two-state simulation, the fundamental levels of the  $\nu_7$  (CCD bend+NN stretch) and  $\nu_6$  (CCC bend+CCN bend) modes of the  $\tilde{A}^2B_1$  state may correspond to peaks *e* and *f*, respectively, while that of the  $\nu_5$  mode (CN stretch+CCC symmetric stretch) of the  $\tilde{X}^2A_2$

state may contribute to peak *e* significantly. In light of the discrepancy between the observed spectrum and the full nonadiabatic simulation, these assignments are considered highly tentative.

Peak *g* is assigned as the fundamental level of the  $\nu_4$  mode (CCC symmetric stretch+NN stretch) of the  $\tilde{X}^2A_2$  state. The  $\beta$  value of peak *g* is very similar to that of peak *a*, the  $^2A_2$  origin peak, in agreement with the assignment. It is noticeable in the simulation that the nonadiabatic interactions result in the splitting of the intensity of the  $\nu_4$  fundamental peak into two resonance peaks.

The simulation also suggests that peak *h* represents the fundamental level of the  $\nu_3$  mode (CN stretch+CCC bend) of the  $\tilde{A}^2B_1$  state. This assignment is consistent with the observed  $\beta$  value. At the higher eBE, many vibronic levels with relatively small intensities contribute to the spectrum. Experimentally, there are no well resolved fine structures observed in the high eBE region. Correspondence between the observed spectrum and the simulation may not be very good in this energy region due to the limited size of the basis set of the model Hamiltonian and the neglect of the higher-order terms in the model potential. Nevertheless, the main features of the observed spectrum are very well reproduced by the nonadiabatic simulation where all three states are fully coupled.

As mentioned earlier, a full nonadiabatic simulation of the 1-pyrazolide- $h_3$  spectrum is computationally unfeasible. Instead, we have studied one-state and two-state simulations and utilized the similarity of the photoelectron spectra of the isotopomers to identify each peak of the 1-pyrazolide- $h_3$  spectrum. The results of our analysis of the nonadiabatic effects in the 1-pyrazolyl- $h_3$  radical are given as supplementary materials.<sup>41</sup>

## IV. DISCUSSION

### A. Spectral simulation with a model Hamiltonian technique

The subject under study in this paper—the photoelectron spectrum of the 1-pyrazolide anion—is a complicated and technically challenging problem; the system has 18 vibrational modes, and the spectrum exhibits profound effects arising from strong nonadiabatic coupling between three closely spaced electronic states. Given these complications, it is truly remarkable that the model Hamiltonian method employed here succeeds in reproducing the experimental spectrum so faithfully. It is especially noteworthy that this congruence of the measured and simulated spectra has been achieved without resort to a procedure in which the Hamiltonian parameters are fit to the spectra. Indeed, apart from a uniform scaling of the model potential parameters,<sup>71</sup> the simulation shown in Fig. 10 is fully *ab initio*.

Historically, the model potential approach of Köppel *et al.* has been applied within the framework of the linear vibronic coupling (LVC) model.<sup>4</sup> In this approach, the quadratic force fields of the final states are not allowed to “relax” from that of the state—usually the absorbing state in the spectroscopic experiments—used to define the normal coordinates and diabatic force field for the problem at hand. Hence, a quantitative reproduction of spectra in which the initial and final states have appreciably different frequencies or normal coordinates is not possible in principle when the LVC model is used. Typically, the parameters of the LVC potential are adjusted to improve agreement with experiment. However, qualitative agreement with experiment—as seen, for example, in studies of the electronic absorption spectrum of pyrazine,<sup>14,15</sup> the photoelectron spectrum of *p*-benzoquinone,<sup>28</sup> and the photodetachment of the nitrate anion<sup>13</sup> to the ground state of NO<sub>3</sub>—is generally adequate to assist in assigning the observed spectra and in understanding general features of the electronic states and their coupling mechanisms.

The quadratic vibronic coupling (QVC) model has seen considerably less application in the literature, becoming commonplace only in recent years.<sup>12,16,19,24–27,78,79</sup> Most previous applications of this method have used an approach akin to the vertical parametrization that was discussed earlier in this paper. As well studied previously for the LVC model,<sup>4</sup> the vertical parametrization has advantages of reproducing the spectral intensity distribution of vibrationally highly excited levels very well.<sup>58,59</sup> This character has made application of the QVC model with the vertical parametrization successful in treating nonadiabatic dynamics, for example, in photoionization of allene,<sup>19</sup> where the conical intersection is located near the vertical geometry. However, the vertical parametrization will give harmonic frequencies that are related to the quadratic force fields of the final states at the absorbing state equilibrium geometry, and anharmonicity associated with the diabatic potentials is completely neglected. Hence, intensities (via mode mixing) and the level structure (via anharmonicity) of the spectrum are compromised. This point is important for the photodetachment of the 1-imidazolidine and 1-pyrazolide anions because only a few vibrational levels, which are located below the conical intersection, are observed in the spectra (Figs. 2 and 4).

In this work, we have introduced a new method for parametrizing the QVC model. While involving more computation than the vertical parametrization procedure, the adiabatic parametrization has a number of practical advantages. Harmonic frequencies of the final state are, by construction, equal to those of the quantum chemical model used in the parametrization procedure, as is the adiabatic energy separation apart from zero-point vibrational energies. Favorable features of the adiabatic parametrization have been noted in a study of the photoelectron spectrum of ozone.<sup>12</sup> In this case, the potential energy surfaces were mapped out from first principles, and the coupling constants were subsequently determined by fitting the model potentials to the *ab initio* surfaces around the final state geometries. Our treatment is essentially the same, except that our potential constants are determined analytically [see Eqs. (5) and (6)].

As mentioned above, the quantitative agreement of the model Hamiltonian simulation (as parametrized by the adiabatic approach) with the 1-pyrazolyl- $d_3$  spectrum is excellent [Fig. 10(b)]. The fact that such an excellent nonadiabatic simulation is obtained without any arbitrary adjustments to the *ab initio* values attests to the quality of both the EOMIP-CCSD method and the model Hamiltonian approach itself. For the systems studied in this paper, the superiority of the adiabatic parametrization relative to the vertical approach is apparent. The issue of parametrization methods associated with the model Hamiltonian technique is irrelevant for spectral simulations using time-dependent quantum wave packet *ab initio* molecular dynamics,<sup>80</sup> where electronic structure calculations are performed “on the fly.” This time-dependent technique has recently been applied to the electronic absorption spectrum of ethylene.<sup>81–83</sup> Such calculations, however, will be extremely expensive for a large molecule such as the pyrazolyl radical, and proper incorporation of nonadiabatic effects into the spectral simulation with *ab initio* molecular dynamics has yet to be explored.

During the course of this investigation, we have found that the simulated spectra are extremely sensitive to the vertical energy spacing of the  ${}^2A_2$  and  ${}^2B_1$  states. Due to the near degeneracy of these two states, many excited vibrational levels of the two states are also quasidegenerate. Hence, shifting the gap by roughly 5–10 meV tends to dramatically affect the appearance of the simulated spectrum, particularly in the vicinity of peaks *e* and *f*.<sup>84,85</sup> This character of nonadiabatic interactions between the  $\tilde{X}{}^2A_2$  and  $\tilde{A}{}^2B_1$  states is important in understanding how the  $\tilde{B}{}^2B_2$  state tends to influence the vibronic structure of the two low-lying states. The coupling between the  $\tilde{B}{}^2B_2$  and  $\tilde{A}{}^2B_1$  states is considerably stronger than that between the  $\tilde{B}{}^2B_2$  and  $\tilde{X}{}^2A_2$  states, resulting in levels belonging to  $\tilde{A}{}^2B_1$  state being lowered much more than those corresponding to the  $\tilde{X}{}^2A_2$  state. The effects of the  $\tilde{B}{}^2B_2$  state on the vibronic structure of the two low-lying states, however, are not just tuning of the relative energies of the relevant levels. Indeed, the  ${}^2B_2$ - ${}^2B_1$  coupling significantly perturbs the vibronic structure of the  $\tilde{A}{}^2B_1$  state, as evidenced by a two-state nonadiabatic simulation of the  $\tilde{B}{}^2B_2$  and  $\tilde{A}{}^2B_1$  states (not shown).

## B. The topology of the potential energy surfaces

Table VIII summarizes information on the adiabatic  $\kappa$  model potentials as well as *ab initio* data for the 1-pyrazolyl radical. Geometries of the  $C_{2v}$  stationary points of the  $\tilde{X}{}^2A_2$ ,  $\tilde{A}{}^2B_1$ , and  $\tilde{B}{}^2B_2$  states of the radical are given relative to the  $\tilde{X}{}^1A_1$  state of the 1-pyrazolide- $d_3$  anion in terms of the reduced normal coordinates of the anion ground state. These equilibrium geometries of the model potentials are, by construction, identical to those optimized with the CCSD/DZP (anion) and EOMIP-CCSD/DZP (neutral) calculations.<sup>41</sup> Also, the relative model potential adiabatic energies of the  ${}^2A_2$ ,  ${}^2B_1$ , and  ${}^2B_2$  states are identical to those from the CCSD(T) calculations by construction. The absolute energy is set by the spectral simulation [Fig. 10(b)]. The vertical

energies are derived from the model potentials based on the CCSD(T) adiabatic energies. We have also located a saddle point in  $C_s$  symmetry with the EOMIP-CCSD/DZP calculations, whose geometry is also given in Table VIII.

As mentioned in Sec. III A, the 1-pyrazolyl radical is isoelectronic with the cyclopentadienyl radical. The nearly degenerate  $\tilde{X}{}^2A_2$  and  $\tilde{A}{}^2B_1$  states of 1-pyrazolyl correspond to the degenerate  $\tilde{X}{}^2E_1'$  states of cyclopentadienyl.<sup>61,62</sup> The linear Jahn-Teller interactions in the  $\tilde{X}{}^2E_1'$  states lead to the formation of a so-called pseudorotation path in the adiabatic potential energy surface.<sup>86</sup> Due to this nonadiabatic interaction, the minimum adiabatic energy points are not located at high symmetry ( $D_{5h}$ ), but at geometries of lowered symmetry ( $C_s$  or  $C_{2v}$ ) along the pseudorotation path. Since the linear Jahn-Teller active modes in  $\tilde{X}{}^2E_1'$  cyclopentadienyl ( $e_2'$  modes) are not active quadratically,<sup>61</sup> there is no potential energy barrier along the pseudorotation path in the absence of any higher-order effects.

The corresponding pseudorotation path in the lowest adiabatic potential energy surface of the 1-pyrazolyl radical finds two minima, i.e., the  $\tilde{X}{}^2A_2$  and  $\tilde{A}{}^2B_1$  stationary points. These two minima are connected through the saddle point of  $C_s$  symmetry shown in Table VIII along the pseudorotation path. The barrier height in adiabatic potential energies (without zero-point energy correction) is 133 meV from the  ${}^2A_2$  minimum and 73 meV from the  ${}^2B_1$  minimum according to the CCSD(T) calculations. In fact, negative quadratic force constants have been found for an  $a'$  mode ( $818i$  cm $^{-1}$ ) and an  $a''$  mode ( $34i$  cm $^{-1}$ ) at the  $C_s$  saddle point with the EOMIP-CCSD calculations. The  ${}^2A_2$  and  ${}^2B_1$  minima can be traced directly along the  $a'$  normal coordinate in the pseudorotation path, while the imaginary frequency of the  $a''$  mode is a reflection of the vibronic coupling with the nearby  $\tilde{B}{}^2B_2$  state.

The nonadiabatic effects of the  $\tilde{B}{}^2B_2$  state on the pseudorotation path can be elucidated through the model potentials. For the sake of arguments, the saddle point geometry is constrained to have a  $C_{2v}$  symmetry; i.e., the displacements from the anion geometry along the  $b_2$  modes shown in Table VIII are ignored. At this  $C_{2v}$ -constrained geometry, the model potentials yield the energies of the  ${}^2A_2$ ,  ${}^2B_1$ , and  ${}^2B_2$  diabatic states to be 3.253, 3.286, and 3.682 eV, respectively; the energy separation between the  ${}^2B_2$  and  ${}^2B_1$  states is 0.396 eV. With this rather small separation, the coupling constant of an  $a_2$  mode ( $\nu_8$ ) is large enough (Table V) to turn the high-symmetry point into a maximum along the normal coordinate for the lower adiabatic potential energy surface. This character must be carried over to the actual saddle point of  $C_s$  symmetry. In the meantime, the energy separation of the  ${}^2B_1$  and  ${}^2A_2$  diabatic states is only 33 meV at the  $C_{2v}$ -constrained geometry. The large vibronic coupling constants for two  $b_2$  modes,  $\nu_{14}$  and  $\nu_{16}$  (Table V), are the driving forces to lower the energy for the lower adiabatic potential energy surface along these normal coordinates, as evident in the  $C_s$  geometry of the saddle point shown in Table VIII.

Of course, pseudorotation paths exist to connect the  ${}^2B_2$  and  ${}^2B_1$  stationary points as well as the  ${}^2B_2$  and  ${}^2A_2$  station-

ary points. The model potentials predict that the energy of the  ${}^2B_1$  state is 0.363 eV above that of the  ${}^2B_2$  state at the  ${}^2B_2$  stationary point. The lower adiabatic potential energy surface finds a negative force constant along an  $a_2$  normal coordinate ( $\nu_8$ ) at the  ${}^2B_2$  stationary point according to the model potential. This character of the model potential is in good agreement with the EOMIP-CCSD calculations (Table I). Thus, along the  ${}^2B_2$ - ${}^2B_1$  pseudorotation path, the  ${}^2B_2$  stationary point is a maximum while the  ${}^2B_1$  stationary point is a minimum. The strong vibronic coupling around the  ${}^2B_2$  stationary point can explain the absence of distinct peaks of  $b_2$  symmetry in the higher eBE region of the simulations in Figs. 9(a) and 10. The situation is similar for the  ${}^2B_2$ - ${}^2A_2$  pseudorotation path.

### C. Conical intersections

Nonadiabatic interactions often play key roles in chemical dynamics. A primary factor that dictates the course of nonadiabatic dynamics are the potential energy surfaces around conical intersections. A few methods have been reported to locate conical intersections of minimum energies via electronic structure calculations.<sup>87,88</sup> In the model potential method, geometries of minimum-energy conical intersections are given in an analytical expression under the LVC model.<sup>4</sup> Here, we utilize the formulation for the LVC model to locate conical intersections with the QVC model.

Two characteristics can be pointed out for minimum-energy conical intersections defined under the LVC model. One is that the energies of the two states are degenerate at the intersections. The other is that when the intersection geometry is defined relative to the equilibrium geometries of the two states in terms of the reference normal coordinates, the corresponding two vectors are parallel (or antiparallel). The former must hold for model potentials of any order. On the other hand, the latter is valid only for the LVC model. However, a corollary of the second feature of minimum-energy conical intersections is that the products of the corresponding harmonic frequencies and the two vectors are also parallel (or antiparallel). The definition of the resultant vectors has a direct analogy to that of the linear intrastate coupling constants [Eq. (5)]. Thus, the “conical intersection (CI)  $\kappa$ ” is defined as the product of the vector representing the geometry difference between the intersection and the neutral equilibrium geometry and the force constant matrix of the corresponding state in terms of the anion reduced normal coordinates. Under the QVC model used in the present study, this force constant matrix accounts for mode mixing, unlike the LVC model where the corresponding matrix is diagonal. The two CI  $\kappa$  are parallel (or antiparallel) at the minimum-energy conical intersections. Practically, the search of the minimum-energy conical intersections is carried out with the intersection under the LVC model as a starting geometry. Then, a vector is calculated based on the corresponding CI  $\kappa$ . This vector is composed of two orthogonal vectors: one represents the energy difference of the two diabatic states, and the other represents the perpendicular component of the difference vector of the two CI  $\kappa$ . A gradient of each component of the vector is calculated numerically for each  $a_1$  mode. The

resultant matrix is inverted and applied back to the original vector to define a new conical intersection geometry following the standard Newton’s method. The solution is obtained iteratively and given in Table VIII. The same procedure can be implemented with the *ab initio* calculations. The corresponding conical intersection information from the *ab initio* calculations is also provided in Table VIII.

The geometry of the conical intersection between the  $\tilde{X}{}^2A_2$  and  $\tilde{A}{}^2B_1$  states clearly indicates that photodetachment from the 1-pyrazolide anion accesses the immediate vicinity of the conical intersection. The model potential energy of the conical intersection is 3.246 eV, which is only 9 meV below the vertical energy of the  ${}^2B_1$  state and 24 meV below that of the  ${}^2A_2$  state. Thus, it is inevitable that the wave packet motion is enormously influenced by the nonadiabatic interactions between the two states in the photodetachment process, considering the large vibronic coupling constants (Table V). The two-state simulation (Fig. 7) certainly demonstrates such huge nonadiabatic effects. The energy of the conical intersection is 0.302 and 0.242 eV higher than those of the  ${}^2A_2$  and  ${}^2B_1$  states at the corresponding minima, respectively, according to the model potentials. These values compare to the adiabatic energy of the conical intersection of  $\tilde{X}{}^2E_1'$  cyclopentadienyl, 0.183 eV, relative to that of the pseudorotation path, calculated at the CASSCF/6-31G\* level of theory.<sup>61,62</sup>

On the other hand, the conical intersections between the  $\tilde{B}{}^2B_2$  and  $\tilde{A}{}^2B_1$  states and between the  $\tilde{B}{}^2B_2$  and  $\tilde{X}{}^2A_2$  states are located farther away from the anion geometry, compared to the  ${}^2A_2$ - ${}^2B_1$  conical intersection. While this geometry comparison implies less importance of the vibronic interaction of the  $\tilde{B}{}^2B_2$  state on the wave packet dynamics in the event of detachment to the  ${}^2A_2$  and  ${}^2B_1$  states, our spectral simulations show significant effects of the coupling with the  ${}^2B_2$  state on the vibronic structure of the  ${}^2A_2$  and  ${}^2B_1$  states.

Wave packet dynamics following detachment to the  ${}^2B_2$  state will be extremely complicated, probably passing through both conical intersection regions. Note particularly the proximity of the  ${}^2B_2$ - ${}^2A_2$  conical intersection and the  ${}^2B_2$  stationary point. Energetically, the model potential conical intersection is only 3 meV above the stationary point. No matter what the wave packet dynamics, our simulations suggest that the resultant spectrum can only exhibit a dense manifold of the vibrational levels (Figs. 9 and 10).

Matsika and Yarkony have recently reported their electronic structure calculations on the 1-pyrazolyl radical system.<sup>30</sup> They have optimized geometries for the  $\tilde{X}{}^2A_2$  and  $\tilde{B}{}^2B_2$  states and computed the energies at the MRCISD/cc-pVDZ level of theory. Their geometries are in good agreement with those optimized with the EOMIP-CCSD/DZP calculations in the present study (EPAPS<sup>41</sup>). They have found the adiabatic energy of the  $\tilde{B}{}^2B_2$  state to be 0.349 eV higher than that of the  $\tilde{X}{}^2A_2$  state (without zero-point vibrational energy correction), compared to 0.287 eV calculated at the CCSD(T)/cc-pVTZ level in the present study (Table VIII). They have applied their algorithm to locate a three-state conical intersection<sup>89</sup> to the pyrazolyl system, and found that

the energy of the three-state conical intersection is 0.426 eV above the adiabatic energy of the  $\tilde{X}^2A_2$  state.<sup>30,31</sup> Our CCSD(T) calculations show that the vertical energies of the  $^2A_2$  and  $^2B_1$  states are 0.327 and 0.354 eV, respectively, relative to the adiabatic energy of the  $\tilde{X}^2A_2$  state (Table II). While the potential energy surfaces around the three-state conical intersection may not be very important to photodetachment to the  $^2A_2$  and  $^2B_1$  states, nuclear dynamics following photodetachment to the  $^2B_2$  state may experience the direct effects of the three-state intersection.

## V. CONCLUSION

The photoelectron spectrum of the 1-pyrazolide- $d_3$  anion has been measured. The photoelectron angular distributions indicate the presence of nearly degenerate electronic states of the 1-pyrazolyl- $d_3$  radical. EOMIP-CCSD calculations have been performed to study the low-lying states of the radical. The calculations strongly suggest that three electronic states, energetically close to each other, are accessed in the photodetachment process. The calculations also find substantial nonadiabatic interactions in each pair of the three states. The effects of the vibronic interactions among the three states are investigated with spectral simulations using a model diabatic Hamiltonian technique. Model potentials have been constructed for the three states as a function of the anion reduced normal coordinates up to quadratic terms. The parameters of the quadratic vibronic coupling (QVC) model potentials have been evaluated based on the EOMIP-CCSD and CCSD(T) calculations using a new analytic method, which is analogous to a procedure used in conventional Franck-Condon overlap calculations. The good quality of the QVC parametrization method, which accounts for the mode mixing effects correctly, has been demonstrated in simulations of the photoelectron spectrum of the 1-imidazolide anion.

The model Hamiltonian simulation successfully reproduces the fine structure of the 1-pyrazolyl- $d_3$  spectrum and reveals the complicated nonadiabatic effects in the spectrum. The ground state of the 1-pyrazolyl- $d_3$  radical is a  $^2A_2$  state, and the electron affinity is  $2.935 \pm 0.006$  eV. The term energy of the first excited state,  $\tilde{A}^2B_1$  state, is  $32 \pm 1$  meV. Reasonable assignments have been made for the observed vibronic peaks, which are consistent with the corresponding photoelectron angular distributions. Particularly strong nonadiabatic interactions between the  $\tilde{X}^2A_2$  and  $\tilde{A}^2B_1$  states are evident in the simulations, while the vibronic interaction with the  $\tilde{B}^2B_2$  state also exerts important effects on the observed vibronic structure for the  $\tilde{X}^2A_2$  and  $\tilde{A}^2B_1$  states. The simulation predicts no distinct peaks of vibrational levels belonging to the  $\tilde{B}^2B_2$  state, even though the state is located within the energy range of the observed spectrum. The absence of such distinct peaks is a result of the strong vibronic interactions with the  $^2A_2$  and  $^2B_1$  states.

The topology of the adiabatic potential energy surfaces of the 1-pyrazolyl radical has been discussed based on the model potentials as well as coupled-cluster calculations. The adiabatic energy of the  $^2B_1$  minimum is 60 meV higher than that of the  $^2A_2$  minimum. The pseudorotation path in the

planar symmetry that connects the two minima finds a saddle point whose energy barrier is 73 meV relative to the  $^2B_1$  minimum. At this  $C_s$  saddle point, an imaginary frequency is found also for an  $a''$  mode, which reflects vibronic interactions with the  $\tilde{B}^2B_2$  state. The minimum-energy conical intersection has been located for the  $\tilde{X}^2A_2$  and  $\tilde{A}^2B_1$  states within the framework of the quadratic vibronic coupling model. The conical intersection is very close to the geometry of the anion ground state, such that photodetachment probes the immediate vicinity of the conical intersection. This proximity, together with large vibronic coupling constants, explains the complexity of nonadiabatic effects in the  $\tilde{X}^2A_2$  and  $\tilde{A}^2B_1$  states. The adiabatic energy of the conical intersection is 0.242 eV relative to the  $^2B_1$  minimum according to the model potentials. In contrast to the  $^2A_2$  and  $^2B_1$  minima, the  $^2B_2$  stationary point is a local maximum as a result of vibronic interactions with the  $^2A_2$  and  $^2B_1$  states.

## ACKNOWLEDGMENTS

We would like to thank Dr. Rebecca L. Hoenigman for her help in the synthesis of the deuterated pyrazole. We are grateful to Dr. Shuji Kato for his help in the mass spectrometric measurements of the deuterated pyrazole sample. Parts of the coupled-cluster calculations and model Hamiltonian calculations were performed with the JILA Keck Cluster supported by the W. M. Keck Foundation. This research was funded by the Air Force Office of Scientific Research, the National Science Foundation, and the Welch Foundation.

- <sup>1</sup>A. J. Gianola, T. Ichino, R. L. Hoenigman, S. Kato, V. M. Bierbaum, and W. C. Lineberger, *J. Phys. Chem. A* **108**, 10326 (2004).
- <sup>2</sup>A. J. Gianola, T. Ichino, R. L. Hoenigman, S. Kato, V. M. Bierbaum, and W. C. Lineberger, *J. Phys. Chem. A* **109**, 11504 (2005).
- <sup>3</sup>A. J. Gianola, T. Ichino, S. Kato, V. M. Bierbaum, and W. C. Lineberger, *J. Phys. Chem. A* **110**, 8457 (2006).
- <sup>4</sup>H. Köppel, W. Domcke, and L. S. Cederbaum, *Adv. Chem. Phys.* **57**, 59 (1984).
- <sup>5</sup>L. S. Cederbaum, W. Domcke, H. Köppel, and W. Vonniessen, *Chem. Phys.* **26**, 169 (1977).
- <sup>6</sup>E. Haller, L. S. Cederbaum, W. Domcke, and H. Köppel, *Chem. Phys. Lett.* **72**, 427 (1980).
- <sup>7</sup>E. Haller, H. Köppel, L. S. Cederbaum, W. Vonniessen, and G. Bieri, *J. Chem. Phys.* **78**, 1359 (1983).
- <sup>8</sup>H. Köppel, L. S. Cederbaum, and W. Domcke, *J. Chem. Phys.* **89**, 2023 (1988).
- <sup>9</sup>J. Eiding, R. Schneider, W. Domcke, H. Köppel, and W. Vonniessen, *Chem. Phys. Lett.* **177**, 345 (1991).
- <sup>10</sup>H. Müller, H. Köppel, L. S. Cederbaum, T. Schmelz, G. Chambaud, and P. Rosmus, *Chem. Phys. Lett.* **197**, 599 (1992).
- <sup>11</sup>H. Müller, H. Köppel, and L. S. Cederbaum, *New J. Chem.* **17**, 7 (1993).
- <sup>12</sup>H. Müller, H. Köppel, and L. S. Cederbaum, *J. Chem. Phys.* **101**, 10263 (1994).
- <sup>13</sup>M. Mayer, L. S. Cederbaum, and H. Köppel, *J. Chem. Phys.* **100**, 899 (1994).
- <sup>14</sup>C. Woywod, W. Domcke, A. L. Sobolewski, and H. J. Werner, *J. Chem. Phys.* **100**, 1400 (1994).
- <sup>15</sup>G. A. Worth, H. D. Meyer, and L. S. Cederbaum, *J. Chem. Phys.* **109**, 3518 (1998).
- <sup>16</sup>A. Raab, G. A. Worth, H. D. Meyer, and L. S. Cederbaum, *J. Chem. Phys.* **110**, 936 (1999).
- <sup>17</sup>A. B. Trofimov, H. Köppel, and J. Schirmer, *J. Chem. Phys.* **109**, 1025 (1998).
- <sup>18</sup>S. Mahapatra, H. Köppel, and L. S. Cederbaum, *J. Chem. Phys.* **110**, 5691 (1999).

- <sup>19</sup> S. Mahapatra, G. A. Worth, H. D. Meyer, L. S. Cederbaum, and H. Köppel, *J. Phys. Chem. A* **105**, 5567 (2001).
- <sup>20</sup> C. Cattarius, G. A. Worth, H. D. Meyer, and L. S. Cederbaum, *J. Chem. Phys.* **115**, 2088 (2001).
- <sup>21</sup> M. Doscher, H. Köppel, and P. G. Szalay, *J. Chem. Phys.* **117**, 2645 (2002).
- <sup>22</sup> H. Köppel, M. Doscher, I. Baldea, H. D. Meyer, and P. G. Szalay, *J. Chem. Phys.* **117**, 2657 (2002).
- <sup>23</sup> J. Schmidt-Klugmann, H. Köppel, S. Schmatz, and P. Botschwina, *Chem. Phys. Lett.* **369**, 21 (2003).
- <sup>24</sup> M. Nooijen, *Int. J. Quantum Chem.* **95**, 768 (2003).
- <sup>25</sup> J. Neugebauer, E. J. Baerends, and M. Nooijen, *J. Phys. Chem. A* **109**, 1168 (2005).
- <sup>26</sup> A. Hazra and M. Nooijen, *Phys. Chem. Chem. Phys.* **7**, 1759 (2005).
- <sup>27</sup> A. Hazra and M. Nooijen, *J. Chem. Phys.* **122**, 204327 (2005).
- <sup>28</sup> J. F. Stanton, K. W. Sattelmeyer, J. Gauss, M. Allan, T. Skalicky, and T. Bally, *J. Chem. Phys.* **115**, 1 (2001).
- <sup>29</sup> Y. J. Bomble, K. W. Sattelmeyer, J. F. Stanton, and J. Gauss, *J. Chem. Phys.* **121**, 5236 (2004).
- <sup>30</sup> S. Matsika and D. R. Yarkony, *J. Am. Chem. Soc.* **125**, 12428 (2003).
- <sup>31</sup> M. S. Schuurman and D. R. Yarkony, *J. Chem. Phys.* **124**, 124109 (2006).
- <sup>32</sup> L. Blancafort and M. A. Robb, *J. Phys. Chem. A* **108**, 10609 (2004).
- <sup>33</sup> J. D. Coe and T. J. Martinez, *J. Am. Chem. Soc.* **127**, 4560 (2005).
- <sup>34</sup> J. D. Coe and T. J. Martinez, *J. Phys. Chem. A* **110**, 618 (2006).
- <sup>35</sup> J. F. Stanton and R. J. Bartlett, *J. Chem. Phys.* **98**, 7029 (1993).
- <sup>36</sup> J. F. Stanton and J. Gauss, *J. Chem. Phys.* **101**, 8938 (1994).
- <sup>37</sup> J. F. Stanton, *J. Chem. Phys.* **115**, 10382 (2001).
- <sup>38</sup> T. E. Sharp and H. M. Rosenstock, *J. Chem. Phys.* **41**, 3453 (1964).
- <sup>39</sup> R. Botter, V. H. Dibeler, J. A. Walker, and H. M. Rosenstock, *J. Chem. Phys.* **44**, 1271 (1966).
- <sup>40</sup> F. Duschinsky, *Acta Physicochim. URSS* **7**, 551 (1937).
- <sup>41</sup> See EPAPS Document No. E-JCPSPA6-125-004634 for supplementary tables, figures, and text. This document can be reached via a direct link in the online article's HTML reference section or via the EPAPS homepage (<http://www.aip.org/pubservs/epaps.html>).
- <sup>42</sup> K. M. Ervin and W. C. Lineberger, in *Advances in Gas Phase Ion Chemistry*, edited by N. G. Adams and L. M. Babcock (JAI, Greenwich, 1992), Vol. 1, p. 121.
- <sup>43</sup> D. G. Leopold, K. K. Murray, A. E. S. Miller, and W. C. Lineberger, *J. Chem. Phys.* **83**, 4849 (1985).
- <sup>44</sup> K. M. Ervin, J. Ho, and W. C. Lineberger, *J. Chem. Phys.* **91**, 5974 (1989).
- <sup>45</sup> T. Andersen, H. K. Haugen, and H. Hotop, *J. Phys. Chem. Ref. Data* **28**, 1511 (1999).
- <sup>46</sup> J. C. Rienstra-Kiracofe, G. S. Tschumper, H. F. Schaefer, S. Nandi, and G. B. Ellison, *Chem. Rev. (Washington, D.C.)* **102**, 231 (2002).
- <sup>47</sup> J. Cooper and R. N. Zare, *J. Chem. Phys.* **48**, 942 (1968).
- <sup>48</sup> J. Elguero, R. Jacquier, V. Pellegrin, and V. Tabacik, *Bull. Soc. Chim. Fr.* **1970**, 1974.
- <sup>49</sup> J. F. Stanton, J. Gauss, J. D. Watts *et al.*, ACES II, a program product of the Quantum Theory Project, University of Florida. Integral packages included are the following: J. Almlof and P. R. Taylor, VMOL; P. R. Taylor, VPROPS; and T. Helgaker, H. J. Aa. Jensen, P. Jorgensen, J. Olsen, and P. R. Taylor, ABACUS.
- <sup>50</sup> G. D. Purvis and R. J. Bartlett, *J. Chem. Phys.* **76**, 1910 (1982).
- <sup>51</sup> E. A. Salter, G. W. Trucks, and R. J. Bartlett, *J. Chem. Phys.* **90**, 1752 (1989).
- <sup>52</sup> J. Gauss and J. F. Stanton, *Chem. Phys. Lett.* **276**, 70 (1997).
- <sup>53</sup> T. H. Dunning, *J. Chem. Phys.* **53**, 2823 (1970).
- <sup>54</sup> L. T. Redmon, G. D. Purvis, and R. J. Bartlett, *J. Am. Chem. Soc.* **101**, 2856 (1979).
- <sup>55</sup> K. Raghavachari, G. W. Trucks, J. A. Pople, and M. Headgordon, *Chem. Phys. Lett.* **157**, 479 (1989).
- <sup>56</sup> T. H. Dunning, *J. Chem. Phys.* **90**, 1007 (1989).
- <sup>57</sup> The CCSD(T) calculations predict that the  ${}^2A_1$  state is adiabatically 1.83 eV above the  ${}^2A_2$  state for the 1-pyrazolyl radical. The  ${}^2A_1$  state is ignored in our treatment.
- <sup>58</sup> L. S. Cederbaum and W. Domcke, *Adv. Chem. Phys.* **36**, 205 (1977).
- <sup>59</sup> W. Domcke, L. S. Cederbaum, H. Köppel, and W. Vonniessen, *Mol. Phys.* **34**, 1759 (1977).
- <sup>60</sup> E. J. Heller, *Acc. Chem. Res.* **14**, 368 (1981).
- <sup>61</sup> B. E. Applegate, T. A. Miller, and T. A. Barckholtz, *J. Chem. Phys.* **114**, 4855 (2001).
- <sup>62</sup> B. E. Applegate, A. J. Bezant, and T. A. Miller, *J. Chem. Phys.* **114**, 4869 (2001).
- <sup>63</sup> The relative signs of  $\lambda$  parameters reflect those of the corresponding normal coordinates. Only the magnitudes are shown in Table V, while the relative signs are apparent in Table VIII.
- <sup>64</sup> J. H. Richardson, L. M. Stephenson, and J. I. Brauman, *J. Chem. Phys.* **59**, 5068 (1973).
- <sup>65</sup> J. H. Richardson, L. M. Stephenson, and J. I. Brauman, *J. Am. Chem. Soc.* **97**, 1160 (1975).
- <sup>66</sup> P. C. Engelking and W. C. Lineberger, *J. Chem. Phys.* **67**, 1412 (1977).
- <sup>67</sup> M. H. Palmer and I. C. Walker, *Chem. Phys.* **157**, 187 (1991).
- <sup>68</sup> M. H. Palmer, I. C. Walker, M. F. Guest, and A. Hopkirk, *Chem. Phys.* **147**, 19 (1990).
- <sup>69</sup> Nontotally symmetric modes can show up only in terms of  $(2\nu) \times n$ , where  $n$  is an integer. The present study does not incorporate anharmonic effects in the adiabatic simulation.
- <sup>70</sup> This observation can be used as a check on the convergence of the model Hamiltonian calculation with respect to the number of Lanczos recursion and basis set size.
- <sup>71</sup> Presumably, this scaling accounts for deficiencies in the treatment of dynamic electron correlation (triples) in the EOMIP-CCSD method. See Y. J. Bomble, J. C. Saeh, J. F. Stanton, P. G. Szalay, M. Kallay, and J. Gauss, *J. Chem. Phys.* **122**, 154107 (2005).
- <sup>72</sup> Certainly, the resonance feature can be reproduced in the adiabatic simulation as long as the anharmonicity of the potential energy surface is taken into account. In the 1-imidazolyl system, the corresponding anharmonicity is associated with one totally symmetric mode (linear) and one vibronic coupling mode (quadratic). Nonadiabatic simulation with quadratic model potentials can accommodate the effects of such anharmonicity as the totally symmetric mode tunes the energy difference of the two vibronically coupled states. See Ref. 2.
- <sup>73</sup> The reduction in the number of vibronic coupling modes is made based on the magnitudes of the linear interstate coupling constants. We assume that the diabatic off-diagonal quadratic force constants, which mix these coupling modes, are zero in the treatment of the model potentials. Indeed, we find negligible off-diagonal elements in the force constant matrix evaluated at the anion geometry once contributions from the vibronic interactions are subtracted. Such observation has been made previously for the *p*-benzoquinone system (Ref. 28). It should be mentioned that the numbers of nuclear basis functions for the totally symmetric modes, on the other hand, cannot be determined simply from the magnitudes of the linear coupling constants because of the mode mixing (see Tables III, IV, and VI).
- <sup>74</sup> The simulation in Fig. 5(c) is not fully converged due to the inadequate size of the basis set. For instance, the positions of the minor peaks associated with two quanta of the  $\nu_6$  mode are shifted by 13 meV from the fully converged spectrum. Augmenting the basis set, however, will prevent us from achieving convergence with respect to the vibronic coupling modes when we study three-state vibronic interactions. Therefore, such an increase in the basis set size is not made here. This truncation does not affect the major spectral features in the adiabatic simulation of the  ${}^2B_2$  state. Furthermore, as we will show later, the main vibronic structure observed in the photoelectron spectrum (Fig. 4) is associated with the vibronic levels belonging to the  ${}^2A_2$  and  ${}^2B_1$  states. Thus, the effects of this truncation on the final three-state simulation are negligible.
- <sup>75</sup> R. F. Gunion, M. K. Gilles, M. L. Polak, and W. C. Lineberger, *Int. J. Mass Spectrom. Ion Process.* **117**, 601 (1992).
- <sup>76</sup> J. Ho, K. M. Ervin, and W. C. Lineberger, *J. Chem. Phys.* **93**, 6987 (1990).
- <sup>77</sup> J. Ho, K. M. Ervin, M. L. Polak, M. K. Gilles, and W. C. Lineberger, *J. Chem. Phys.* **95**, 4845 (1991).
- <sup>78</sup> A. Hazra and M. Nooijen, *Int. J. Quantum Chem.* **95**, 643 (2003).
- <sup>79</sup> A. Hazra, H. H. Chang, and M. Nooijen, *J. Chem. Phys.* **121**, 2125 (2004).
- <sup>80</sup> M. Ben-Nun and T. J. Martinez, *Adv. Chem. Phys.* **121**, 439 (2002).
- <sup>81</sup> M. Ben-Nun and T. J. Martinez, *J. Phys. Chem. A* **103**, 10517 (1999).
- <sup>82</sup> K. K. Baeck and T. J. Martinez, *Chem. Phys. Lett.* **375**, 299 (2003).
- <sup>83</sup> H. C. Choi, K. K. Baeck, and T. J. Martinez, *Chem. Phys. Lett.* **398**, 407 (2004).
- <sup>84</sup> This high sensitivity may imply that a more elaborate treatment of vibronic coupling modes in the model potentials is necessary to provide a more correct representation of the spectral feature of peaks *e* and *f*.
- <sup>85</sup> This aspect of the nonadiabatic simulation also indicates the importance of zero-point vibrational energies. In the present study, the quadratic cou-

pling constants for the vibronic coupling modes are evaluated at the anion geometry, which may result in small deviation from true zero-point energies. For those nontotally symmetric modes that do not participate in vibronic coupling (e. g.,  $a_2$  modes for the  ${}^2A_2$  state), the quadratic coupling constants are evaluated from the harmonic vibrational frequencies of the anion and neutral states under the parallel mode approximation.

- <sup>86</sup>T. A. Barckholtz and T. A. Miller, *Int. Rev. Phys. Chem.* **17**, 435 (1998).  
<sup>87</sup>M. J. Bearpark, M. A. Robb, and H. B. Schlegel, *Chem. Phys. Lett.* **223**, 269 (1994).  
<sup>88</sup>D. R. Yarkony, in *Modern Electronic Structure Theory, Part I*, edited by D. R. Yarkony (World Scientific, Singapore, 1995), p. 642.  
<sup>89</sup>S. Matsika and D. R. Yarkony, *J. Chem. Phys.* **117**, 6907 (2002).